

A Discrete Fiber Dispersion Model with Octahedral Symmetry Quadrature for Applications in Skin Mechanics

Riccardo Alberini^a, Michele Terzano^b, Gerhard A. Holzapfel^{b,c}, Andrea Spagnoli^{a,*}

^a*Department of Engineering and Architecture, University of Parma, Parma, Italy*

^b*Institute of Biomechanics, Graz University of Technology, Graz, Austria*

^c*Department of Structural Engineering, Norwegian University of Science and Technology, Trondheim, Norway*

Abstract

Advanced simulations of the mechanical behavior of soft tissues frequently rely on structure-based constitutive models, including smeared descriptions of collagen fibers. Among them, the so-called Discrete Fiber Dispersion (DFD) model is based on a discrete integration of the fiber-strain energy over all the fiber directions. In this paper, we recall the theoretical framework of the DFD model, including a derivation of the stress and stiffness tensors required for the finite element implementation. Specifically, their expressions for incompressible plane stress problems are obtained. The use of a Lebedev quadrature, built exploiting the octahedral symmetry, is then proposed, illustrating the particular choice adopted for the orientation of the integration points. Next, the convergence of this quadrature scheme is assessed by means of three numerical benchmark tests, highlighting the advantages with respect to other angular integration methods available in the literature. Finally, we propose as applicative example a simulation of Z-plasty, a technique commonly used in reconstructive skin surgery, considering multiple geometrical configurations and orientations of the fibers. Results are provided in terms of key mechanical quantities relevant for the surgical practice.

Keywords: skin mechanics, anisotropy, angular integration, discrete fiber dispersion model, Lebedev quadrature.

1. Introduction

In recent years, the development of structure-based mechanical models has gained significant attention in computational mechanics, particularly for materials with a complex internal microstructure such as soft collagenous tissues. These models aim to capture the non-linear and anisotropic material behavior more accurately with respect to purely phenomenological formulations, by accounting for the non-uniform dispersion of the fibers within the material [1]. Tissues such as arterial walls, heart valves,

*Corresponding author

Tel.: +39 0521 905927

e-mail: spagnoli@unipr.it

gastric muscle, and skin are mainly constituted by a dispersion of wavy collagen fibers embedded in a ground isotropic substance [2–5]. The orientation distribution of the fibers in the three-dimensional space is given by a Probability Density Function (PDF), which can be included in the constitutive model according to two main approaches: the Generalized Structure Tensor (GST) and the Angular Integration (AI) approaches [6]. In the GST approach, the PDF is used to calculate a structure tensor representative of the fiber distribution, which is then used in the strain-energy function to determine a pseudo-invariant accounting for the anisotropy. Based on a specific shape of the PDF, the structure tensor can be computed in a closed form, without requiring further integration during the analysis. For this reason, models based on this approach, such as those proposed by Merodio and Ogden [7], Gasser et al. [8], Holzapfel et al. [9] to name a few, became popular due to their computational efficiency [1].

A downside of these models is that they cannot exclude the contribution of compressed fibers along individual directions without compromising the computational efficiency, since all the fibers directions are *a priori* included. Latorre and Montáns [10] showed that the criterion originally chosen for excluding the compressed fibers, which is based on the mean direction [8], may produce nonphysical discontinuities in the stress–strain behavior. They proposed a new pre-integrated method, although limited to axially symmetric fiber distributions. Melnik et al. [11], Li et al. [12] introduced a GST-based model in which the structure tensor is integrated accounting for the stretched fibers only, but since the computation is required at each deformation the efficiency of the original model is compromised. On the other hand, in the AI approach, also referred to as Continuous Fiber Dispersion (CFD) [13], the PDF is used to weigh the integration of the single fiber strain-energy over all the directions, allowing for a simple fiber exclusion criterion during the computation, and independent of the shape of the PDF. However, this comes with a compromise on the computational efficiency, since the integration must be performed multiple times during the analysis.

In an effort to increase the computational performance while preserving the advantages of the AI approach, an hybrid approach named Discrete Fiber Dispersion (DFD) model was introduced, based on a discrete integration over the spherical domain of the fibers [13]. In this method, the choice of the integration scheme plays a fundamental role and can significantly affect the mechanical response. Li et al. [13] originally proposed an integration method based on the discretization of the unit sphere with uniform triangular areas, each associated to a discrete fiber orientation with a weight computed by exactly integrating the PDF over the relative area. The method has been optimized by Rolf-Pissarczyk et al. [14] who developed an adaptive meshing to locally discretize the unit sphere surface with finer elements where the values of the PDF are concentrated. However, this method tends to increase the number of integration points for fiber distribution approaching the perfect alignment, while in such case only few representative directions would be sufficient. Moreover, there is little control on the number of integration points, since the refinement bisects spherical triangular elements until all the weights attain a value lower than a specified threshold.

In the light of the above, alternative quadrature schemes appear a valid choice for the integration due

to their versatility for selecting the level of precision and the number of points [15]. Notable examples include methods proposed by Bažant and Oh [16], Fliege and Maier [17], Heo and Xu [18]. There are mathematical requirements that need to be satisfied. To ensure poly-convexity of the strain-energy function [19], integration points should not be associated to negative coefficients [20]. Moreover, the distribution of the points over the sphere should be as uniform as possible in order to maximize the integration efficiency, as well as to attain the invariance of the integral under general rotations of the integration points [20, 21]. The number of points also plays a crucial role, since schemes with reduced points may induce anisotropic behaviors for isotropic materials, as pointed out by Ehret et al. [20]. Lastly, since stress, strain, and related kinematic variables have identical values at diametrically opposite points on the sphere, centrally symmetric integration schemes are favored. They indeed allow the integral to be computed over only half of the sphere, effectively reducing the number of integrand evaluations by half [22]. Recently, Britt and Ehret [23] proposed an approach based on the transformation of the spherical integral over the unit sphere into a linear integral over the distribution of the stretch of the fibers, which can be easily computed using a n -point Gauss quadrature.

According to the findings of Ehret et al. [20], who compared the performance of different integration schemes, quadrature schemes based on the construction of a spherical grid with polyhedral symmetry showed great potential in terms of computational efficiency and accuracy. In particular, the Lebedev rule, built exploiting octahedral symmetry [24, 25], demonstrated to perform the best out of the nine methods tested by Skacel and Bursa [21]. However, only elementary loading cases were considered, and further analyses including complex loading configurations are required to investigate the convergence rate, as well as the ideal number of integration points for efficient Finite Element (FE) simulations. To this aim, in the present work, we address the numerical performance of the quadrature scheme with both elementary and advanced benchmark tests in large deformations. Specifically, we analyze the homogeneous uniaxial tension and simple shear tests, and the isotropic annular disk subjected to torsion of the internal boundary. The tests conducted confirm that the Lebedev quadrature exhibits rapid convergence to the exact solution, validating its suitability for high-fidelity mechanical simulations. The analyses were performed in the commercial FE software Abaqus [26].

As an applicative example of the DFD model considered, we show a Z-plasty simulation, which has great relevance in skin mechanics. Z-plasty involves making Z-shaped incisions to release tension and improve the mobility of the skin, particularly in areas of scarring or contracture [27]. While the procedure is widely used in clinical practice, its application is largely guided by empirical experience rather than by a quantitative understanding of the underlying mechanics. If not correctly executed, these surgeries could potentially worsen the existing conditions, with the consequent need of further and more risky interventions. Therefore, a preoperative inspection is extremely important, and surgeons must assess key factors such as skin quality, underlying bone structure, vascular supply, extension of the defect, and direction of the natural skin tension. By combining this information the surgeon can determine the appropriate technique and plan the operation, as well as inform the patient about risks and possible outcomes [28]. In

this regard, several surgical guidelines can be found in the literature [29–31], some of which providing an algorithmic approach to determine the most suitable technique depending on factors such as the defect length, skin availability or skin tension [32]. However, these guidelines all lack quantitative mechanical evidences.

Recent works of Buganza Tepole et al. [33] and Stowers et al. [34] extensively analyzed similar surgical procedures, providing valuable mechanical insights that could help refine surgical practices, shifting from empirically driven decisions to more data-informed approaches. Following the same approach, in this work the DFD model is applied to simulate Z-plasty for various incision configurations and fiber orientations, providing novel insights into the mechanical behavior of the skin after the procedure. The simulation results can provide support for surgical practice, especially in terms of optimizing incision placement and orientation relative to the collagen fiber architecture of the skin. For example, the findings suggest that certain incision angles with respect to the mean collagen direction lead to reduced post-operative strain, thus improving healing outcomes. These results not only enhance the understanding of Z-plasty mechanics but also pave the way for more personalized and optimized surgical strategies.

The paper is organized as follows. In Section 2 the theoretical framework of the DFD model is presented, including the derivation of the stress and stiffness tensors required for the FE implementation, and their specific formulation for incompressible plane stress problems. The Lebedev quadrature scheme is then introduced, illustrating the particular choice for the orientation of the integration points. Next, the convergence of the quadrature is assessed by means of numerical benchmark tests. In Section 4 the Z-plasty is simulated for multiple geometrical configurations and orientations of the fibers. Results are provided in terms of key mechanical quantities relevant for the surgical practice. In Section 5 some considerations about the implemented model and the Z-plasty results are addressed, while in Section 6 the conclusions are drawn.

2. Mechanical modeling

2.1. Description of general fiber distributions

Let $\rho(\mathbf{N}) = \rho(\theta, \phi)$ be the Probability Density Function (PDF) defined over the unit sphere $\mathbb{S} = \{(\theta, \phi) \mid \theta \in [-\pi, \pi], \phi \in [-\pi/2, \pi/2]\}$. The PDF provides the normalized collagen fiber density in the direction of the unit vector \mathbf{N} in the reference configuration,

$$\mathbf{N}(\theta, \phi) = \cos \phi \cos \theta \mathbf{E}_1 + \cos \phi \sin \theta \mathbf{E}_2 + \sin \phi \mathbf{E}_3, \quad (1)$$

where $\{\mathbf{E}_1, \mathbf{E}_2, \mathbf{E}_3\}$ defines the Cartesian unit vectors basis (Fig. 1(a)), while θ and ϕ represent the azimuth and elevations angles, respectively. Since a fiber in the direction \mathbf{N} is also represented by the opposite vector $-\mathbf{N}$, we require the PDF to satisfy the symmetry $\rho(\mathbf{N}) = \rho(-\mathbf{N})$, or equivalently $\rho(\theta, \phi) = \rho(\theta + \pi, -\phi)$.

We now assume the PDF to be a combination of a finite number m of fiber families each described by an independent PDF $\rho_i(\mathbf{N})$ as

$$\rho(\mathbf{N}) = \sum_{i=1}^m \nu_i \rho_i(\mathbf{N}) , \quad (2)$$

where ν_i represents the normalized volume fraction of the i -th fiber family, with $\sum \nu_i = 1$, and each $\rho_i(\mathbf{N})$ must satisfy the normalization condition over the unit sphere \mathbb{S}

$$\frac{1}{4\pi} \int_{\mathbb{S}} \rho_i(\mathbf{N}) dS = \frac{1}{4\pi} \int_{-\pi}^{\pi} \int_{-\pi/2}^{\pi/2} \rho_i(\theta, \phi) \cos \phi d\theta d\phi = 1 . \quad (3)$$

To account for general orientations of each fiber family in the Euclidean space we then introduce the principal orthonormal unit vectors basis $\{\mathbf{M}_i, \mathbf{M}_{\text{ip},i}, \mathbf{M}_{\text{op},i}\}$ (Fig. 1(b)), in which \mathbf{M}_i represents the preferential direction of the family, $\{\mathbf{M}_i, \mathbf{M}_{\text{ip},i}\}$ defines its mean plane, and $\mathbf{M}_{\text{op},i}$ is the out-of-plane normal. The rotation of this basis relative to the global basis $\{\mathbf{E}_k\}_{k=1,2,3}$ is described by the triplet of angles $\alpha_i, \beta_i, \gamma_i$, where the first two denote the azimuthal and elevation angle of the mean fiber direction, $\mathbf{M}_i = \mathbf{N}(\alpha_i, \beta_i)$, while the last one represents the rotation of the basis about \mathbf{M}_i (Fig. 1(c)). Accordingly, based on experimental evidences on biological tissues [35, 36], the PDF ρ_i is assumed to be decoupled into two independent univariate PDFs as

$$\rho_i(\mathbf{N}) = \rho_{\text{ip},i}(\mathbf{N}) \rho_{\text{op},i}(\mathbf{N}) , \quad (4)$$

in which $\rho_{\text{ip},i}(\mathbf{N})$ and $\rho_{\text{op},i}(\mathbf{N})$ describe, respectively, the in-plane and out-of-plane distributions with respect to the basis $\{\mathbf{M}_i, \mathbf{M}_{\text{ip},i}, \mathbf{M}_{\text{op},i}\}$. Following the work of Holzapfel et al. [9], we specialize the two functions employing two π -periodic von Mises distributions of the form

$$\rho_{\text{ip},i}(\mathbf{N}) = \frac{\exp[a_i(2(\mathbf{N}_{\text{ip}} \cdot \mathbf{M}_i/|\mathbf{N}_{\text{ip}}|)^2 - 1)]}{I_0(a_i)} , \quad (5)$$

$$\rho_{\text{op},i}(\mathbf{N}) = 2\sqrt{\frac{2b_i}{\pi}} \frac{\exp[-2b_i(\mathbf{N} \cdot \mathbf{M}_{\text{op},i})^2]}{\text{erf}(\sqrt{2b_i})} , \quad (6)$$

where the vector \mathbf{N}_{ip} represent the projection of \mathbf{N} onto the plane $\{\mathbf{M}_i, \mathbf{M}_{\text{ip},i}\}$. The functions $I_0(\bullet)$ and $\text{erf}(\bullet)$ are the modified Bessel function of the first kind of order zero and the error function of (\bullet) , respectively, which ensure the normalization condition (3). The constants a_i and b_i are parameters that define the in-plane and out-of-plane concentrations, respectively. Thus, using Eqs. (2) and (4) each fiber family is fully described by the set of parameters $\{a_i, b_i, \alpha_i, \beta_i, \gamma_i, \nu_i\}$. The limit case of $a_i, b_i \rightarrow \infty$ corresponds to perfect fiber alignment along \mathbf{M}_i , while for $a_i, b_i \rightarrow 0$ an isotropic distribution is obtained (Fig. 2(a)). Negative values are also admissible, but describe a fiber distribution no longer concentrated in the direction \mathbf{M}_i . For instance, $a_i = 0$ and $b_i < 0$ represent an axially symmetric fiber distribution

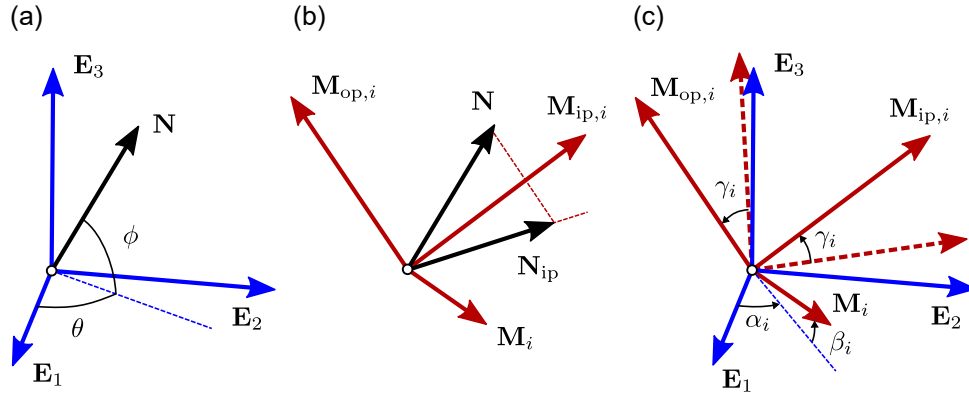


Figure 1. Schematic representation of the orientation of the unit vector \mathbf{N} (in black), the global Cartesian basis $\{\mathbf{E}_1, \mathbf{E}_2, \mathbf{E}_3\}$ (in blue) and the principal orthonormal basis $\{\mathbf{M}_i, \mathbf{M}_{ip,i}, \mathbf{M}_{op,i}\}$ (in red) of the fiber family. (a) Unit vector \mathbf{N} in the global frame; (b) unit vector \mathbf{N} in the principal fiber family basis and its projection \mathbf{N}_{ip} onto the mean fiber plane $\{\mathbf{M}_i, \mathbf{M}_{ip,i}\}$; (c) rotation of the principal basis with respect to the global basis using the angles $\alpha_i, \beta_i, \gamma_i$. Dashed vectors represent $\mathbf{M}_{ip,i}$ and $\mathbf{M}_{op,i}$ before the rotation about \mathbf{M}_i .

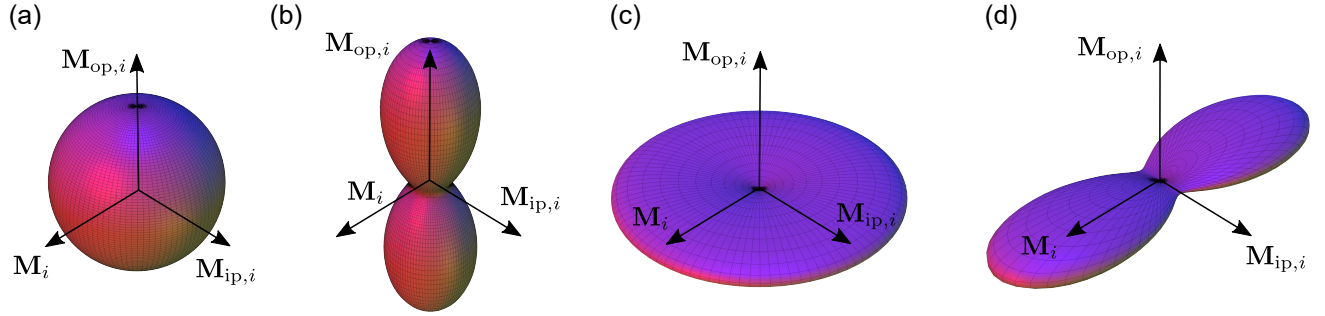


Figure 2. Polar representation of representative von Mises distributions. (a) Isotropic distribution, $a_i, b_i \rightarrow 0$; (b) axially symmetric distribution, $a_i = 0$ and $b_i < 0$; (c) quasi-planar isotropic distribution $a_i = 0, b_i \rightarrow \infty$; (d) general distribution $a_i, b_i > 0$.

with preferential direction along $\mathbf{M}_{op,i}$ (Fig. 2(b)). The particular choice for the distributions in Eqs. (5) and (6) verifies symmetry requirement $\rho_i(\mathbf{N}) = \rho_i(-\mathbf{N})$, and has the additional in-plane and out-of-plane symmetries about \mathbf{M}_i .

2.2. Constitutive model

Let $\mathbf{F} = \partial \mathbf{x}(\mathbf{X}) / \partial \mathbf{X}$ be the deformation gradient describing the deformation field in the neighborhood of a material point moving from the position \mathbf{X} in the reference configuration to a position \mathbf{x} in the current configuration. The change in length and direction of a fiber in the direction of the unit vector \mathbf{N} in the reference configuration can then be expressed as $\mathbf{F}\mathbf{N} = \lambda \mathbf{n}$, where λ is the stretch ratio and \mathbf{n} is the unit vector of the new fiber direction in the current configuration. Accordingly, the square of the fiber stretch is expressed by the invariant $I_4 = \lambda^2 = \mathbf{C} : \mathbf{N} \otimes \mathbf{N}$, with $\mathbf{C} = \mathbf{F}^T \mathbf{F}$ denoting the right Cauchy-Green tensor.

Following the DFD approach, we describe the mechanical behavior of a single fiber family by approximating the overall strain-energy function of the continuous fiber dispersion as [13]

$$\Psi_{f,i} = \frac{1}{4\pi} \int_{\mathbb{S}} \rho_i(\mathbf{N}) \Psi_{\text{sf}}(I_4) dS \approx \sum_{j=1}^n w_j \rho_i(\mathbf{N}_j) \Psi_{\text{sf}}(I_{4,j}), \quad (7)$$

where \mathbf{N}_j and w_j , $j = 1, \dots, n$, are the integration points and weights defined by the specific integration scheme over the unit sphere \mathbb{S} , respectively, Ψ_{sf} is the single-fiber strain-energy function, and $I_{4,j} = \mathbf{C} : \mathbf{N}_j \otimes \mathbf{N}_j$ is the squared stretch of a fiber in the direction of \mathbf{N}_j . In general, the number n of integration points can be different for each fiber family. To exclude the negligible contribution of the compressed fibers, the single-fiber strain-energy function $\Psi_{\text{sf}}(I_{4,j})$ is defined as

$$\Psi_{\text{sf}}(I_{4,j}) = \begin{cases} f(I_{4,j}) & I_{4,j} \geq 1, \\ 0 & I_{4,j} < 1, \end{cases} \quad (8)$$

adopting the exponential function proposed by Holzapfel et al. [37], i.e.

$$f(I_{4,j}) = \frac{c_1}{2c_2} \left\{ \exp [c_2(I_{4,j} - 1)^2] - 1 \right\}. \quad (9)$$

in which the two constants c_1 and c_2 represents the stiffness-like parameter and the stiffening parameter of the fibers, respectively.

The mechanical behavior of the isotropic ground matrix embedding the collagen fibers is described using the neo-Hookean model, whose strain-energy function reads

$$\Psi_{\text{g}} = \frac{\mu}{2} (I_1 - 3), \quad (10)$$

where $I_1 = \mathbf{C} : \mathbf{I}$ is the first invariant of \mathbf{C} , \mathbf{I} is the second-order identity tensor, and μ is the initial shear modulus.

Assuming material incompressibility, a common assumption in models of soft biological materials [38], the total strain-energy function Ψ is obtained by additively combining the energy contributions of the ground matrix and of the fiber families weighed with their respective volume fractions ν_i , i.e.

$$\Psi = \Psi_{\text{g}} + \sum_{i=1}^m \nu_i \Psi_{f,i} - p(J - 1), \quad (11)$$

where the last term depending on the volume ratio $J = \det(\mathbf{F})$ is a penalty function introduced to enforce perfect incompressibility ($J = 1$), in which the Lagrange multiplier p assumes the meaning of an unknown hydrostatic pressure.

2.3. Stress and stiffness tensors for incompressible plane stress formulations

The implementation of the model (11) into a FE code requires the stress and stiffness tensors to be explicitly computed.

The second Piola-Kirchhoff stress tensor \mathbf{S} is obtained by differentiation of Eq. (11) with respect to $\frac{1}{2}\mathbf{C}$. Since both J and p are dependent on \mathbf{C} , the tensor reads [39]

$$\mathbf{S} = 2\frac{\partial\Psi}{\partial\mathbf{C}} = 2\left[\Psi'_g(I_1)\mathbf{I} + \sum_{i=1}^m \nu_i \sum_{j=1}^n \varrho_{i,j} \Psi'_{\text{sf}}(I_{4,j})\mathbf{N}_j \otimes \mathbf{N}_j\right] - 2\frac{\partial p}{\partial\mathbf{C}}(J-1) - pJ\mathbf{C}^{-1}, \quad (12)$$

with $\Psi'_\diamond(\diamond)$ denoting the first derivative of Ψ_\diamond with respect to \diamond , and $\varrho_{i,j} = w_j\rho_i(\mathbf{N}_j)$ is introduced for shorter notation. Note that the term containing the derivative of p , even though it would vanish for $J=1$, is kept to ensure the full derivation of the spherical component of the stiffness tensor [39]. By a Piola transformation on \mathbf{S} the Cauchy stress tensor $\boldsymbol{\sigma}$ can be obtained as

$$\boldsymbol{\sigma} = J^{-1}\mathbf{F}\mathbf{S}\mathbf{F}^T = 2J^{-1}\left[\Psi'_g(I_1)\mathbf{b} + \sum_{i=1}^m \nu_i \sum_{j=1}^n \varrho_{i,j} \Psi'_{\text{sf}}(I_{4,j})\mathbf{n}_j \otimes \mathbf{n}_j\right] - 2J^{-1}\mathbf{b}\frac{\partial p}{\partial\mathbf{b}}(J-1) - p\mathbf{I}, \quad (13)$$

where $\mathbf{b} = \mathbf{F}\mathbf{F}^T$ is the left Cauchy-green tensor, and $\mathbf{n}_j = \mathbf{F}\mathbf{N}_j$.

Further differentiation of Eq. (12) with respect to $\frac{1}{2}\mathbf{C}$ gives the tangent elasticity tensor \mathbb{C} in Lagrangian description

$$\begin{aligned} \mathbb{C} = 2\frac{\partial\mathbf{S}}{\partial\mathbf{C}} = & 4\left[\Psi''_g(I_1)\mathbf{I} \otimes \mathbf{I} + \sum_{i=1}^m \nu_i \sum_{j=1}^n \varrho_{i,j} \Psi''_{\text{sf}}(I_{4,j})\mathbf{N}_j \otimes \mathbf{N}_j \otimes \mathbf{N}_j \otimes \mathbf{N}_j\right] + \\ & - 4\frac{\partial^2 p}{\partial\mathbf{C}\partial\mathbf{C}}(J-1) - 2J\left(\frac{\partial p}{\partial\mathbf{C}} \otimes \mathbf{C}^{-1} + \mathbf{C}^{-1} \otimes \frac{\partial p}{\partial\mathbf{C}}\right) + \\ & + 2pJ\mathbf{C}^{-1} \odot \mathbf{C}^{-1} - pJ\mathbf{C}^{-1} \otimes \mathbf{C}^{-1}, \end{aligned} \quad (14)$$

with $\Psi''_\diamond(\diamond)$ denoting the second derivative of Ψ_\diamond with respect to \diamond , and the operator \odot defining the symmetric dyadic product between two second order tensors, $(\odot \odot \bullet)_{ijkl} = 1/2((\odot)_{ik}(\bullet)_{jl} + (\odot)_{il}(\bullet)_{jk})$. Similarly to Eq. (13), a push-forward transformation of the fourth-order tensor \mathbb{C} gives the tangent elasticity tensor \mathbb{c} in spatial description [40]

$$\begin{aligned} \mathbb{c} = J^{-1}\chi_*(\mathbb{C}) = & J^{-1}4\left[\Psi''_g(I_1)\mathbf{b} \otimes \mathbf{b} + \sum_{i=1}^m \nu_i \sum_{j=1}^n \varrho_{i,j} \Psi''_{\text{sf}}(I_{4,j})\mathbf{n}_j \otimes \mathbf{n}_j \otimes \mathbf{n}_j \otimes \mathbf{n}_j\right] + \\ & - 4J^{-1}\mathbf{b}\frac{\partial^2 p}{\partial\mathbf{b}\partial\mathbf{b}}\mathbf{b}(J-1) - 2\left(\mathbf{b}\frac{\partial p}{\partial\mathbf{b}} \otimes \mathbf{I} + \mathbf{I} \otimes \frac{\partial p}{\partial\mathbf{b}}\mathbf{b}\right) + \\ & + 2p\mathbf{I} \odot \mathbf{I} - p\mathbf{I} \otimes \mathbf{I}. \end{aligned} \quad (15)$$

For general three-dimensional problems the pressure p is unknown and it is treated as an independent solution variable commonly solved with a hybrid FE formulation [41]. For plane stress problems, assuming the basis vectors $\mathbf{E}_1, \mathbf{E}_2$ laying in the mean plane, the explicit expression of the pressure p can be derived from Eq. (13) imposing the constraints $\sigma_{33} = \boldsymbol{\sigma} : (\mathbf{E}_3 \otimes \mathbf{E}_3) = 0$ and $J = 1$, namely

$$p = \tilde{\boldsymbol{\sigma}} : (\mathbf{E}_3 \otimes \mathbf{E}_3) = 2J^{-1} \left[\Psi'_g(I_1)(\mathbf{b})_{33} + \sum_{i=1}^m \nu_i \sum_{j=1}^n \varrho_{i,j} \Psi'_{sf}(I_{4,j})(\mathbf{n}_j \otimes \mathbf{n}_j)_{33} \right], \quad (16)$$

with $\tilde{\boldsymbol{\sigma}} = \boldsymbol{\sigma} + p\mathbf{I}$ denoting the deviatoric component of the Cauchy stress. The derivatives of p in Eq. (15) can then be explicitly computed from Eq. (16) giving

$$\mathbf{b} \frac{\partial p}{\partial \mathbf{b}} = \frac{\partial p}{\partial \mathbf{b}} \mathbf{b} = \frac{1}{2} (\mathbf{E}_3 \otimes \mathbf{E}_3) : \tilde{\mathbf{c}} - \frac{1}{2} p \mathbf{I} + p \mathbf{E}_3 \otimes \mathbf{E}_3, \quad (17)$$

where $\tilde{\mathbf{c}}$ is the deviatoric component of the spatial stiffness tensor, represented by the terms within the square brackets in Eq. (15). The second derivative of p in Eq. (15) is not computed since the relevant term vanishes for $J = 1$.

2.4. Implementation into Abaqus FE software

The model presented in Section 2.2 and Section 2.3 has been implemented in the commercial FE software Abaqus through the user-defined subroutine UMAT.

According to the implicit solver formulation (Abaqus/Standard) for plane stress elements, the tensors to be defined are the Cauchy stress, as provided in Eq. (13), and the tangent stiffness tensor $\overset{\circ}{\mathbf{c}}$ relative to the Jaumann rate of the Kirchhoff stress $\overset{\circ}{\boldsymbol{\tau}} = \mathbf{c} : \mathbf{d} + \mathbf{d}\boldsymbol{\tau} + \boldsymbol{\tau}\mathbf{d} = \overset{\circ}{\mathbf{c}} : \mathbf{d}$ [42, 43], i.e.

$$\overset{\circ}{\mathbf{c}} = \mathbf{c} + \boldsymbol{\tau} \odot \mathbf{I} + \mathbf{I} \odot \boldsymbol{\tau}, \quad (18)$$

where $\mathbf{d} = \text{symm}(\dot{\mathbf{F}}\mathbf{F}^{-1})$ is the rate of deformation tensor, and $\boldsymbol{\tau} = J\boldsymbol{\sigma}$ is the Kirchhoff stress tensor.

Since only the planar strain components are used in the plane stress formulation, the transverse deformation $(\mathbf{C})_{33}$ is statically condensed and eliminated from the problem. Accordingly, the coefficients of the statically condensed stiffness tensor $\hat{\mathbf{c}}$ are obtained as [39]

$$(\hat{\mathbf{c}})_{ijkl} = (\overset{\circ}{\mathbf{c}})_{ijkl} - \frac{(\overset{\circ}{\mathbf{c}})_{ij33}(\overset{\circ}{\mathbf{c}})_{33kl}}{(\overset{\circ}{\mathbf{c}})_{3333}}. \quad (19)$$

Additionally, the model has been implemented for perfectly incompressible 3D problems in hybrid formulation. For this case, the Cauchy stress tensor and the full stiffness tensor in Eq. (18) have been defined into the subroutine using only their deviatoric components $\tilde{\boldsymbol{\sigma}}$ and $\tilde{\mathbf{c}}$, respectively. The spherical components are not required, since they are computed by the Abaqus/Standard solver as part of the problem using the hydrostatic pressure variable p .

The special functions $I_0(\bullet)$ and $\text{erf}(\bullet)$ needed to compute the distributions in Eqs. (5) and (6) are incorporated in the UMAT subroutine using the Fortran codes provided by Zhang and Jin [44].

2.5. Model integration scheme

For the numerical integration of Eq. (7) we adopted the Lebedev quadrature rule. The integration points \mathbf{N}_j of this scheme are placed on the surface of the unit sphere forming a grid with octahedral rotational and inversion symmetries about a given orthonormal basis $\{\mathbf{L}_k\}_{k=1,2,3}$, while the relative weights w_j , as well as the number of points n , are determined by enforcing the exact integration of all the spherical harmonics up to a specific degree. Thus, the order of the integration is defined by the degree of the exactly integrated spherical harmonic. To date, Lebedev quadratures have been solved for degrees up to 131, corresponding to $n = 5810$ integration points [25]. In contrast to methods based on the Cartesian product of one-dimensional integrations which cause points to densify near the poles, such as the Gaussian quadrature, Lebedev quadratures yield an even distribution of points across the sphere, as shown in Fig. 3 for $n = 974$. As a result, the number of points per unit area is approximately the same over the unit sphere, thereby enhancing the computational efficiency [21, 45]. Another important aspect of this approach is that the weights w_j are always positive, ensuring the poly-convexity of the solution. In fact, if any weights were negative, the integration could lead to unrealistic results, like negative stresses, when the deformations is all concentrated along a point with negative weight.

For functions different from a spherical harmonic, the Lebedev quadrature provides an approximation of the exact integral, with accuracy improving as the order of the integration increases. Moreover, as for all quadratures, the integral should ideally remain invariant under rigid rotations of the set of integration points relative to the integrand function. With reference to Eq. (7), this implies that any rotation of the basis $\{\mathbf{L}_k\}_{k=1,2,3}$ relative to the global basis $\{\mathbf{E}_k\}_{k=1,2,3}$ yields theoretically the same result. Therefore, without loss of generality, we align $\{\mathbf{L}_k\}_{k=1,2,3}$ with the principal fiber basis $\{\mathbf{M}_i, \mathbf{M}_{\text{ip},i}, \mathbf{M}_{\text{op},i}\}$, so that the integration points \mathbf{N}_j and the distribution $\rho_i(\mathbf{N})$ share the same symmetries. This makes the mechanical response perfectly symmetrical for symmetric deformations about the principal fiber basis, thus ensuring the consistency of the results. Moreover, this guarantees the existence of a point \mathbf{N}_j for every vector of the principal fiber basis. Such a property is useful for nearly perfectly aligned fiber distributions, where the mechanical response is dominated by the integration point \mathbf{N}_j aligned with the mean fiber direction, which can be either \mathbf{M}_i for $a, b \rightarrow \infty$, or $\mathbf{M}_{\text{op},i}$ for $a = 0, b \rightarrow -\infty$.

By exploiting the symmetry $\rho_i(\mathbf{N}) = \rho_i(-\mathbf{N})$ discussed in Section 2.1, we can reduce the computational cost by restricting the integration to only one half of the spherical domain \mathbb{S} . The number of integration points can be further reduced by eliminating the directions \mathbf{N}_j associated to a negligible fiber density, e.g. $\varrho_{i,j} = w_j \rho_i(\mathbf{N}_j) < 10^{-6}$. In this way, as the fiber concentration increases, the number of significant directions \mathbf{N}_j reduces, degenerating to only one direction for a perfectly aligned fiber distribution.

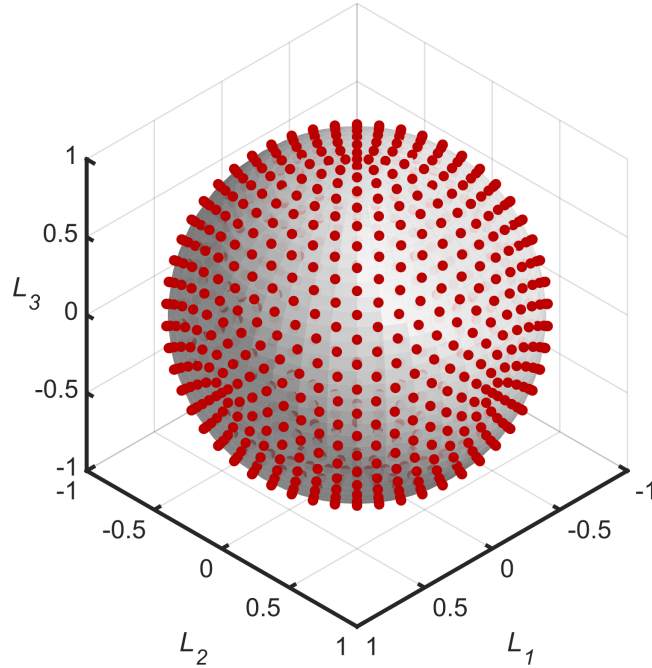


Figure 3. Representative spherical grid of $n = 2 \times 487$ Lebedev integration points in the basis $\{\mathbf{L}_k\}_{k=1,2,3}$.

3. Benchmark tests for convergence assessment

The number n of integration points must be carefully selected to balance computational efficiency and accurate results. To this end, we analyzed the convergence rate of representative problems to the reference solution in relation to the integration order. Specifically, we considered two simple cases of a uniaxial and a simple shear test using a single fiber family with given distribution parameters, and a benchmark torsion test on an annular disk with planar isotropic fiber distribution. For each case we considered integration orders defined by $n = 55, 97, 151, 175, 217, 295, 385, 487, 601, 727$ points over one hemisphere of the unit sphere. For comparison, in the uniaxial and simple shear tests we also included the results of the DFD model computed using the adaptive integration rule proposed by Rolf-Pissarczyk et al. [14]. The points were generated using the MATLAB script provided by the authors. Since the number of points cannot arbitrarily defined, we obtained three sets of integration points with $n = 100, 292, 808$, by varying the threshold value for $q_{i,j}$.

3.1. Uniaxial tension

In this case, we considered a unit square plane stress element (Abaqus CPS4 element) extended along the \mathbf{E}_1 direction by a stretch $\lambda = 1.2$. The material parameters were taken from Alberini et al. [5], with mechanical constants $\mu = 1.142$ kPa, $c_1 = 1.9074$ kPa, $c_2 = 43.6$, and fiber concentrations $a_1 = 2.06$, $b_1 = 12.36$, obtained by averaging the microstructural parameters of human skin (Ref [5] Table 2, Fiber family 1). The fibers were oriented in the direction of the stretch, such that $\mathbf{M}_1 = \mathbf{E}_1$

($\alpha_1 = \beta_1 = \gamma_1 = 0^\circ$). We used as reference solution the CFD model of Li et al. [46], which provides the components of the Cauchy stress tensor derived from the exact integration of Eq. (7). For a uniaxial tests along the \mathbf{E}_1 direction, the analytical expression of the Cauchy stress σ_1 , accounting for the non-symmetrical in-plane and out-of-plane fiber dispersions as defined in Eq. (4), reads

$$\sigma_1 = (\mu + Y_1) \lambda^2 - \sqrt{(\mu + Y_2)(\mu + Y_3)} \lambda^{-1}, \quad (20)$$

with

$$Y_1 = \frac{1}{\pi} \int_{\Sigma} \rho(\theta, \phi) \Psi'_{\text{sf}}(I_4(\theta, \phi)) \cos^3 \phi \cos^2 \theta \, d\theta d\phi, \quad (21)$$

$$Y_2 = \frac{1}{\pi} \int_{\Sigma} \rho(\theta, \phi) \Psi'_{\text{sf}}(I_4(\theta, \phi)) \sin^2 \phi \cos \phi \, d\theta d\phi, \quad (22)$$

$$Y_3 = \frac{1}{\pi} \int_{\Sigma} \rho(\theta, \phi) \Psi'_{\text{sf}}(I_4(\theta, \phi)) \cos^3 \phi \sin^2 \theta \, d\theta d\phi, \quad (23)$$

where $\Sigma = \{\theta \in [-\pi, \pi], \phi \in [-\pi/2, \pi/2] \mid I_4(\theta, \phi) > 1\}$. The deformation-dependent coefficients given in Eqs. (21) to (23) are solved numerically using a MATLAB script with the built-in function `integral2`. As shown in Fig. 4(a) for a representative integration with $n = 727$, the result of the DFD model is in perfect agreement with the CFD model solution.

The convergence rates of the DFD model integrated using the Lebedev quadrature and the adaptive integration rule Rolf-Pissarczyk et al. [14] are reported in Fig. 4(b). For the Lebedev quadrature the error rapidly decreases from about 7.1% for $n = 55$ to 0.03% for $n = 217$, and then it settles at 0.025% for higher integration orders. The adaptive integration also reduces the error with n , but at a slower convergence rate. Notably, as shown in Fig. 4(b), the effective number of points used, by excluding the direction \mathbf{N}_j with negligible influence, is almost reduced by half for all the quadratures considered.

3.2. Simple shear

In this case, we applied a displacement on the top edge of a unit square plane stress element (Abaqus CPS4 element) in the \mathbf{E}_1 direction for an amount of shear of $F_{12} = 0.4$. The material parameters are the same used in the uniaxial test in Section 3.1. To enhance the exclusion of the fibers in compression, we oriented the fiber family at $\alpha_1 = 135^\circ$, while keeping $\beta_1 = \gamma_1 = 0^\circ$. As previously, we used the CFD model as reference solution, for which the analytical expression of the Cauchy shear stress component σ_{12} is given by

$$\sigma_{12} = (\mu + Y_4) F_{12} + Y_3, \quad (24)$$

with

$$Y_4 = \frac{1}{\pi} \int_{\Sigma} \rho(\theta, \phi) \Psi'_{\text{sf}}(I_4(\theta, \phi)) \cos^3 \phi \sin \theta \cos \theta \, d\theta d\phi, \quad (25)$$

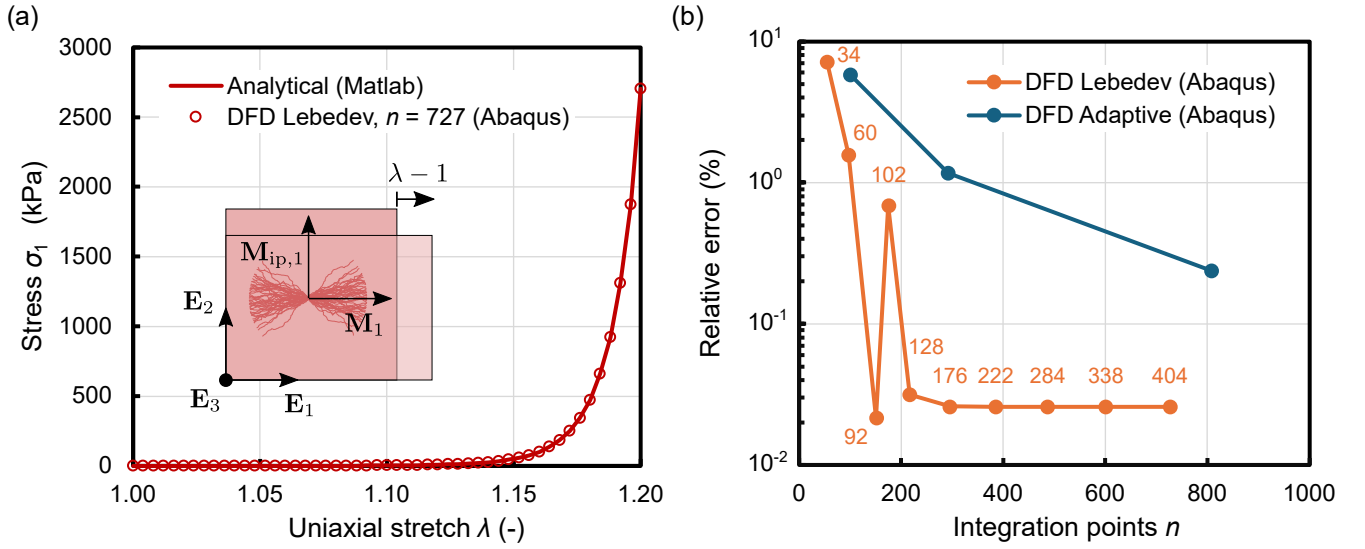


Figure 4. DFD model convergence assessment for a unit square element in uniaxial tension. (a) Cauchy stress σ_1 versus the stretch λ from the CFD model solution in Eq. (20) (solid line) and the representative DFD model solution with $n = 727$ (circles) for the set of mechanical parameters $\mu = 1.142$ kPa, $c_1 = 1.9074$ kPa, $c_2 = 43.6$, and fiber distribution parameters $a_1 = 2.06$, $b_1 = 12.36$, $\alpha_1 = \beta_1 = \gamma_1 = 0^\circ$. A sketch of the uniaxial test is also reported, showing a schematic representation the fiber distribution orientation in relation to the unit square element. (b) Convergence rate of the DFD model implemented in Abaqus relative to the reference CFD solution computed in MATLAB for the Lebedev quadrature rule (orange dots) and the Adaptive integration scheme of Rolf-Pissarczyk et al. [14] (blue dots). Orange numbers indicate the effective number of integration points used, satisfying the condition $\varrho_{i,j} = w_j \rho_i(\mathbf{N}_j) \geq 10^{-6}$.

where, again, the coefficients Y_3 from Eq. (23) and Y_4 are computed numerically over the domain $\Sigma = \{\theta \in [-\pi, \pi], \phi \in [-\pi/2, \pi/2] | I_4(\theta, \phi) > 1\}$ using a MATLAB script with the built-in function `integral2`. The representative result for $n = 727$, and the reference CFD model solution are shown in Fig. 5(a).

In Fig. 5(b) are reported the convergence rates of the DFD model integrated using the Lebedev quadrature and the adaptive integration rule. As for the uniaxial case, the Lebedev quadrature rapidly converges, settling at an error of 0.026% after $n = 217$. For the adaptive integration the error initially increases from 0.21% for $n = 100$ to 0.82% for $n = 292$, but then it stabilizes. The effective numbers of integration points shown in Fig. 5(b) are the same as in the uniaxial tension test, since the same fiber distribution was used.

3.3. Torsion of isotropic annular disk

Beside the convergence rate to the exact solution, a crucial aspect of quadrature schemes, as pointed out by Ehret et al. [20], concerns the invariance of the integration upon rigid rotations of the points \mathbf{N}_j about the integrand function. In fact, for quadratures with a poor number of integration points, the rotation of the basis $\{\mathbf{L}_k\}_{k=1,2,3}$ relative to the integrand function influences the result of the integration,

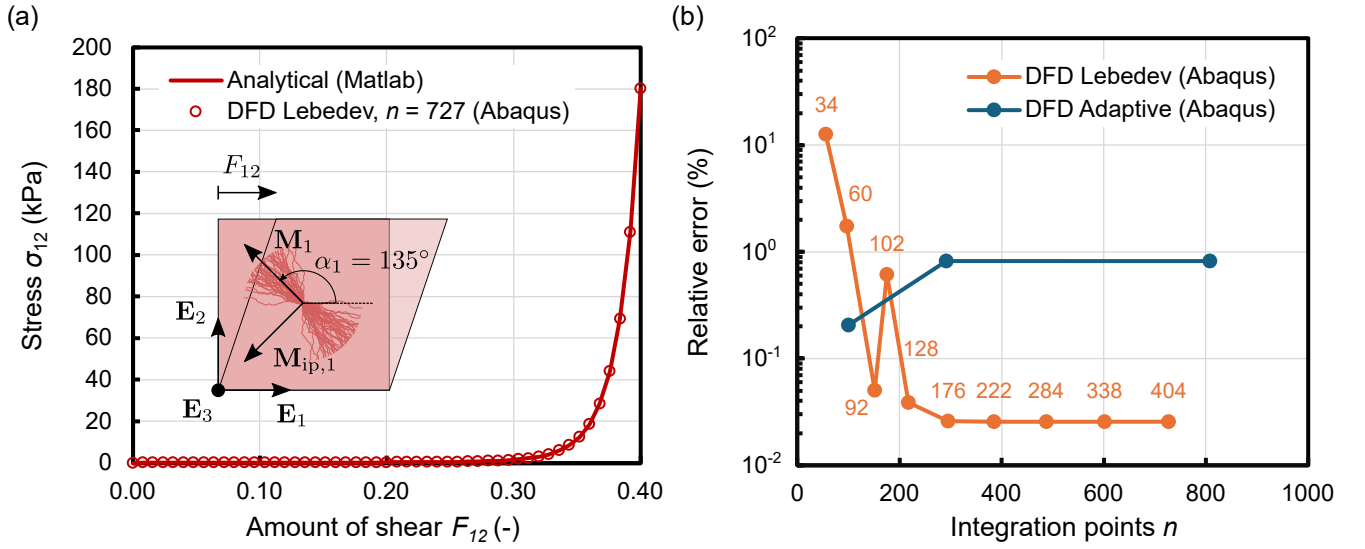


Figure 5. DFD model convergence assessment for a unit square element in simple shear. (a) Stress σ_{12} versus the amount of shear F_{12} plots of the CFD model solution in Eq. (24) (solid line) and the representative DFD model solution with $n = 727$ (circles) for the set of mechanical parameters $\mu = 1.142$ kPa, $c_1 = 1.9074$ kPa, $c_2 = 43.6$, and fiber distribution parameters $a_1 = 2.06$, $b_1 = 12.36$, $\alpha_1 = 135^\circ$, $\beta_1 = \gamma_1 = 0^\circ$. A sketch of the shear test is also reported, showing a schematic representation the fiber distribution orientation in relation to the unit square element. (b) Convergence rate of the DFD model implemented in Abaqus relative to the reference CFD model solution computed in MATLAB for the Lebedev quadrature rule (orange dots) and the Adaptive integration scheme of Rolf-Pissarczyk et al. [14] (blue dots). Orange numbers indicate the effective number of integration points used, satisfying the condition $\varrho_{i,j} = w_j \rho_i(\mathbf{N}_j) \geq 10^{-6}$.

thereby altering the mechanical response, which could become anisotropic for isotropic materials [20, 21]. Conversely, as the number of integration points increases, the quadrature should return the same result regardless the orientation of $\{\mathbf{L}_k\}_{k=1,2,3}$.

To examine the rotational invariance with respect to the number of points n , one can analyze rotations of either the basis $\{\mathbf{L}_k\}_{k=1,2,3}$ or the integrand function while keeping the basis fixed. Since in Section 2.5 we restricted $\{\mathbf{L}_k\}_{k=1,2,3}$ to be coaxial with the principal fiber basis $\{\mathbf{M}_i, \mathbf{M}_{ip,i}, \mathbf{M}_{op,i}\}$, we then decided to analyze an axisymmetric problem in which a quasi-planar isotropic fiber distribution remains fixed throughout the whole domain Ω , while the integrand function of Eq. (7) rotates with the local cylindrical basis $\{\mathbf{E}_r, \mathbf{E}_\vartheta, \mathbf{E}_3\}$ with no dependency on ϑ . Specifically, following Ehret et al. [20], we considered an annular disk with inner radius $R_{in} = 4$ mm, outer radius $R_{out} = 10$ mm, and thickness $t = 0.5$ mm. The disk was discretized with 4-node plane stress elements (Abaqus CPS4 element), using 360 and 49 elements in the circumferential and radial direction, respectively. A counter-clockwise rotation of $\varepsilon = 30^\circ$ was applied to the inner boundary $\partial\Omega_{in}$ while keeping its radial displacements fixed, as well as all the displacements of the outer boundary $\partial\Omega_{out}$, constrained. Mechanical parameters were the same used in the previous tests, using the concentration parameters $a_1 = 0$ and $b_1 = 12.36$ to represent a quasi-planar isotropic fiber dispersion, similar to that shown in Fig. 2(c). Since the integration points

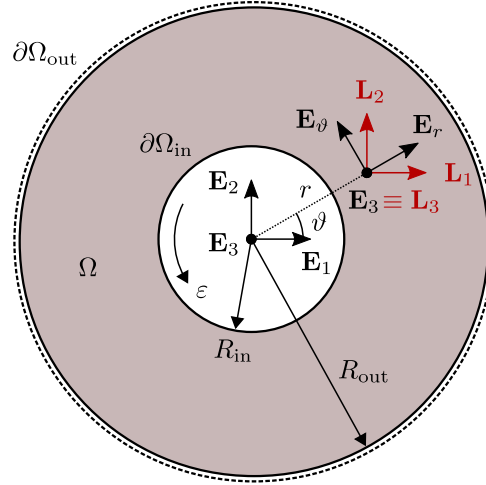
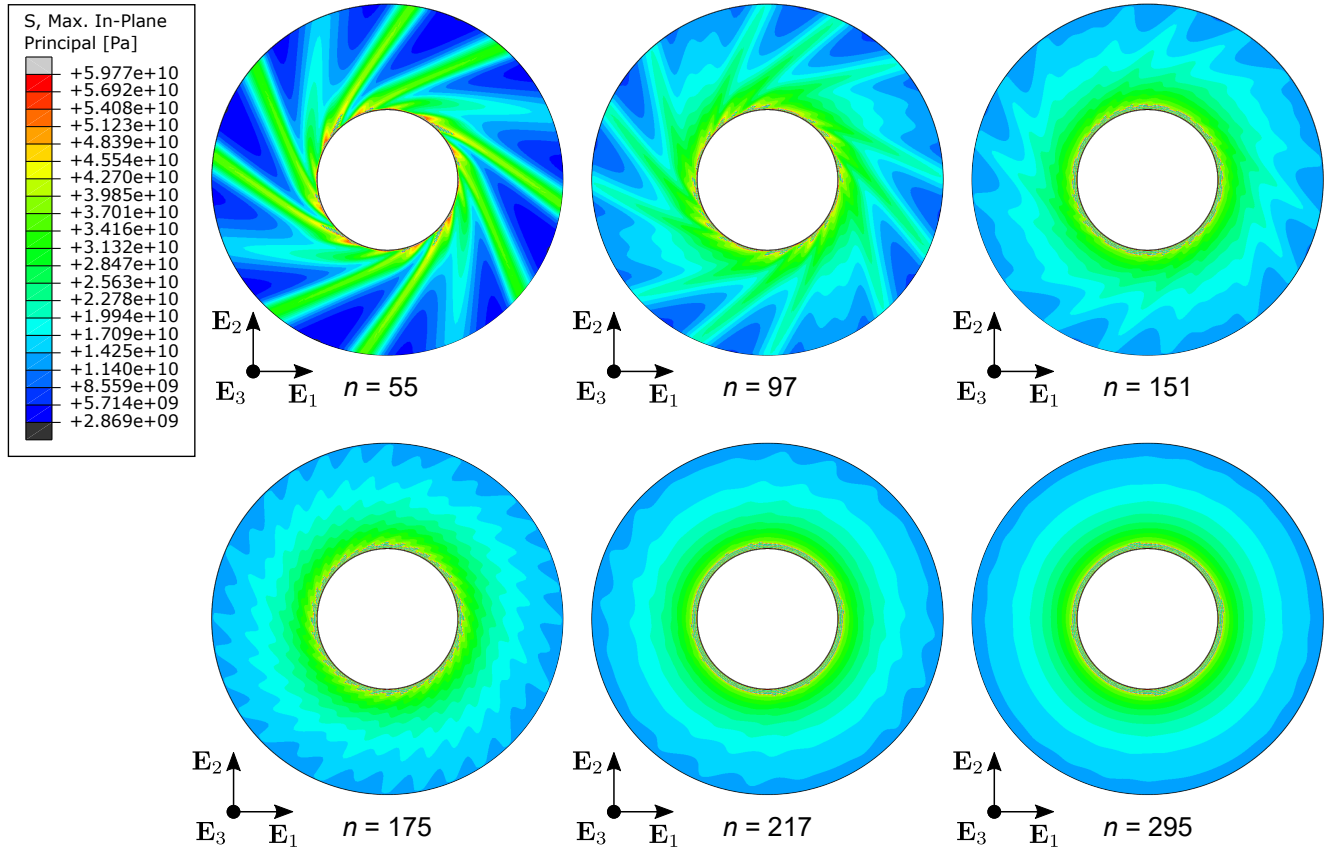


Figure 6. Torsion of an annular disk with respect to the vector \mathbf{E}_3 . The outer boundary $\partial\Omega_{\text{out}}$ is constrained in the radial and tangential directions, indicated with a dashed line, while the inner boundary $\partial\Omega_{\text{in}}$ is left-rotated by $\varepsilon = 30^\circ$ about \mathbf{E}_3 , keeping fixed the radial displacement. The basis of the integration points $\{\mathbf{L}_k\}_{k=1,2,3} \equiv \{\mathbf{M}_i, \mathbf{M}_{\text{ip},i}, \mathbf{M}_{\text{op},i}\}$ is aligned with $\{\mathbf{E}_k\}_{k=1,2,3}$ over the domain Ω . Due to the quasi-planar isotropic distribution chosen for the fibers, $a_1 = 0$, $b_1 = 12.36$, the integrand function in Eq. (7) evaluated with respect to the local cylindrical basis $\{\mathbf{E}_r, \mathbf{E}_\vartheta, \mathbf{E}_3\}$ is independent on the angle ϑ .

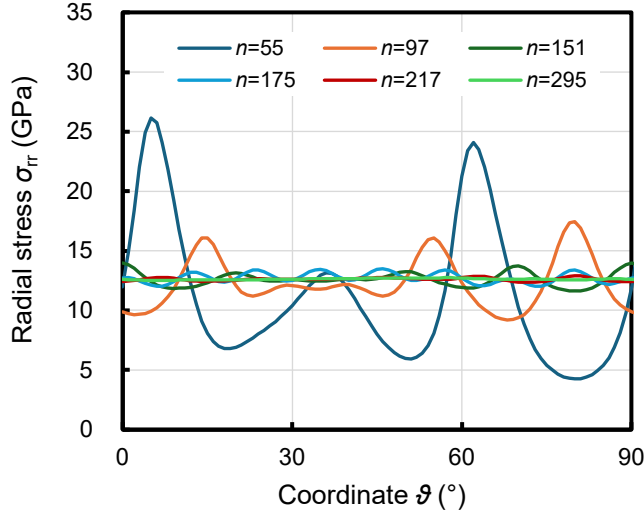
remain fixed, the choice for the fiber distribution is arbitrary. We then used $\alpha_1 = \beta_1 = \gamma_1 = 0^\circ$, such that $\{\mathbf{L}_k\}_{k=1,2,3} \equiv \{\mathbf{E}_k\}_{k=1,2,3}$.

As it can be observed in Fig. 7(a), showing the contour maps of the maximum principal Cauchy stress, the result obtained with low integration orders is strongly non-symmetric, exhibiting several directions of anisotropy. However, as the order increases, further directions of anisotropy develop, approaching to the limit a condition of perfect axial symmetry. To study the convergence rate to the isotropic solution, we analyzed the radial component σ_{rr} of the Cauchy stress over the circular path of radius $R = 7$ mm. Due to the octahedral symmetry of the integration points, the profiles of the stress are $\pi/2$ -periodic, and hence they are reported in Fig. 7(b) for the first six quadratures on the interval $0 \leq \vartheta \leq \pi/2$. Because no analytical solution to this problem is available, we computed the error as the average relative deviation of $\sigma_{rr}(\vartheta)$ from its mean value, such that for the axisymmetric (isotropic) solution the error is exactly zero. The plot of convergence rate, reported in Fig. 7(c), shows a significant reduction of the relative error with n , and attains values lower than 1% for $n \geq 217$. The effective number of integration points, also reported in Fig. 7(c), was substantially reduced for all the quadratures.

(a)



(b)



(c)

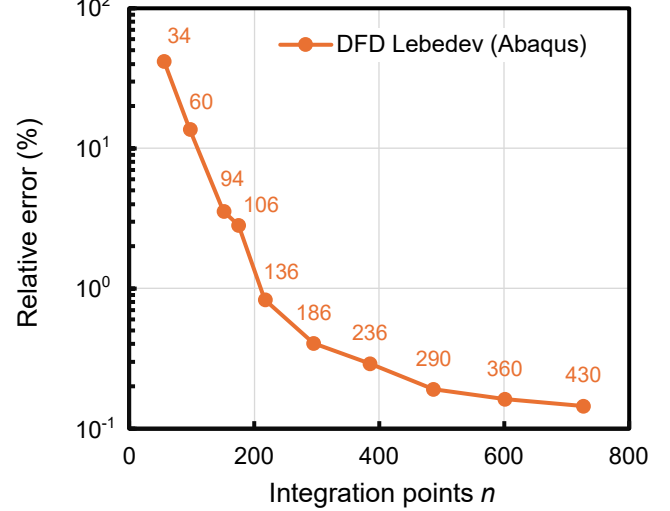


Figure 7. Rotational invariance assessment of the DFD model for an annular disk with mechanical parameters $\mu = 1.142$ kPa, $c_1 = 1.9074$ kPa, $c_2 = 43.6$, and a quasi-planar fiber distribution with concentrations $a_1 = 0$, $b_1 = 12.36$, and orientations $\alpha_1 = \beta_1 = \gamma_1 = 0^\circ$. (a) Contour map of the maximum principal Cauchy stress (Pa) for the first six set of integration points; (b) plots of radial Cauchy stress σ_{rr} versus coordinate ϑ along the circular path with radius $R = 7$ mm for the models shown in (a). Since all $\sigma_{rr}(\vartheta)$ have a period of $\pi/2$, only the interval $0 \leq \vartheta \leq \pi/2$ is shown. (c) Convergence rate of the DFD model to the isotropic solution. The error is evaluated in terms of average relative deviation of $\sigma_{rr}(\vartheta)$ from its mean value.

4. Applicative example: Z-plasty simulation

The traditional Z-plasty in skin surgery consists of three incisions of equal length. The central incision is aligned along the direction of the skin contraction, such as a linear scar or an extended burn scar. The other two incisions extend from either end of the central line in opposite directions at equal angles of 60° to the central line, forming two identical, but opposed, triangular flaps. When these flaps are delaminated from the subcutaneous tissues, they are raised and transposed before suturing to create a new configuration resembling an inverted Z, where the central line becomes perpendicular to the original incision. This procedure increases the distance between the two ends of the initially vertical incision, thus releasing the contraction. The angles of the lateral incision can be adjusted to obtain the desired level of vertical elongation [47]. Generally, larger angles result in greater elongation, but also higher localized deformations, usually correlated to the onset of complications like the distal necrosis [48, 49].

In this section we analyze a set of Z-plasties with incision angle, or triangular flap amplitude, ranging from 20° to 90° , representing an extension of the range in which these surgeries are usually performed in clinical procedures. To understand the influence of the collagen fibers, each set is analyzed for different mean fiber orientation α_1 . The results are then shown and discussed in terms of key mechanical quantities.

4.1. FE model

With reference to the scheme reported in Fig. 8(a), we considered a Z-plasty with vertical and lateral incisions of length $l = 50$ mm in a circular domain of radius $R = 300$ mm. The size for domain is not representative of real operations but is chosen to minimize boundary effects. For numerical purposes, the edges of the cuts were separated by a gap of $s = 0.5$ mm. The angles δ taken into consideration for the analysis were selected from the interval $20^\circ \leq \delta \leq 90^\circ$ at steps of 5° , leading to a set of 15 models. Each domain in the study is discretized using three-node plane stress isoparametric elements (Abaqus CPS3 element), with a maximum size $h_{\max} = l/5$ in regions far from the incisions, progressively reducing to a minimum size $h_{\min} = l/150$ near areas of geometrical discontinuities, such as the cut tips. The outer boundary is assumed to be constrained in all directions. To simulate the closure and the suturing of the skin flaps, the nodes belonging to one side of the internal boundary are linked pairwise to the nodes on the other side, in a way similar to real stitches in surgical procedures. Using a kinematic multi-point constraint, the paired nodes are progressively joined, until the perfect coincidence is achieved. This approach spontaneously finds the final configuration of the suture, which is in general unknown before the analysis. Due to the complexity of adapting the mesh to the application of the multi-point constraints on the internal boundary, the FE models were generated using the algorithm described in Alberini et al. [50]. An example of generated domain for $\delta = 60^\circ$ is reported Fig. 8(b).

Simulations were performed using the average parameters for human skin from Alberini et al. [5], also used in Section 3. In particular, thickness $t = 2.92$ mm, mechanical parameters $\mu = 1.142$ kPa, $c_1 = 1.907$ kPa, $c_2 = 43.6$, and concentrations parameters $a_1 = 2.06$, $b_1 = 12.36$, were used. The fiber distribution was assumed to lie in the mean membrane plane, with out-of-plane angle $\beta_1 = 0^\circ$ and

rolling angle $\gamma_1 = 0^\circ$. Concerning the mean in-plane fiber orientation, six different angles are considered, namely $\alpha_1 = 0^\circ, 30^\circ, 60^\circ, 90^\circ, 120^\circ, 150^\circ$.

Considering the results of Section 3, we used the Lebedev quadrature with $n = 217$ for all the simulations, representing the minimum number of points with relative error below 1% in the annular disk analysis.

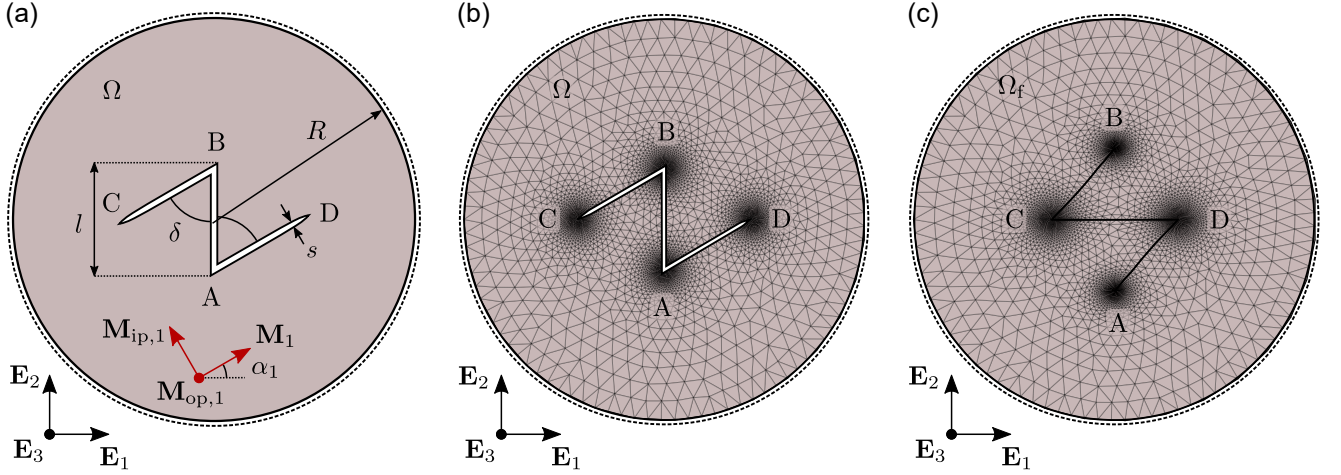


Figure 8. Representative scheme of the Z-plasty model. (a) Geometrical parameters; (b) discretized FE model for $\delta = 60^\circ$ in the reference configuration, and (c) in the final configuration.

4.2. Results

The fundamental measure to evaluate the performance of the Z-plasty is the vertical elongation strain ε_v parallel to the \mathbf{E}_2 direction, defined as

$$\varepsilon_v = \frac{(\Delta \mathbf{x}_v - \Delta \mathbf{X}_v) \cdot \mathbf{E}_2}{\|\Delta \mathbf{X}_v\|}, \quad (26)$$

where $\Delta \mathbf{X}_v = \mathbf{X}_B - \mathbf{X}_A$ and $\Delta \mathbf{x}_v = \mathbf{x}_B - \mathbf{x}_A$ are the distance vectors between the two points A and B of the scar in the reference and current configurations (see Fig. 8(a) and (b) for reference). The horizontal shortening strain ε_h is also considered, namely

$$\varepsilon_h = \frac{(\Delta \mathbf{X}_h - \Delta \mathbf{x}_h) \cdot \mathbf{E}_1}{\|\Delta \mathbf{X}_v\|}, \quad (27)$$

where $\Delta \mathbf{X}_h = \mathbf{X}_D - \mathbf{X}_C$ and $\Delta \mathbf{x}_h = \mathbf{x}_D - \mathbf{x}_C$ are the distance vectors between the two side points C and D of the surgery in the reference and current configurations (see Fig. 8(a) and (b) for reference). Note that ε_h is normalized with respect to $\|\Delta \mathbf{X}_v\|$, and not $\|\Delta \mathbf{X}_h\|$ as one would intuitively assume. The motivation behind this choice is that the initial positions \mathbf{X}_C and \mathbf{X}_D can vary between different surgeries as a function of the opening angle δ and the flap lengths, and normalizing with respect to $\|\Delta \mathbf{X}_h\| =$

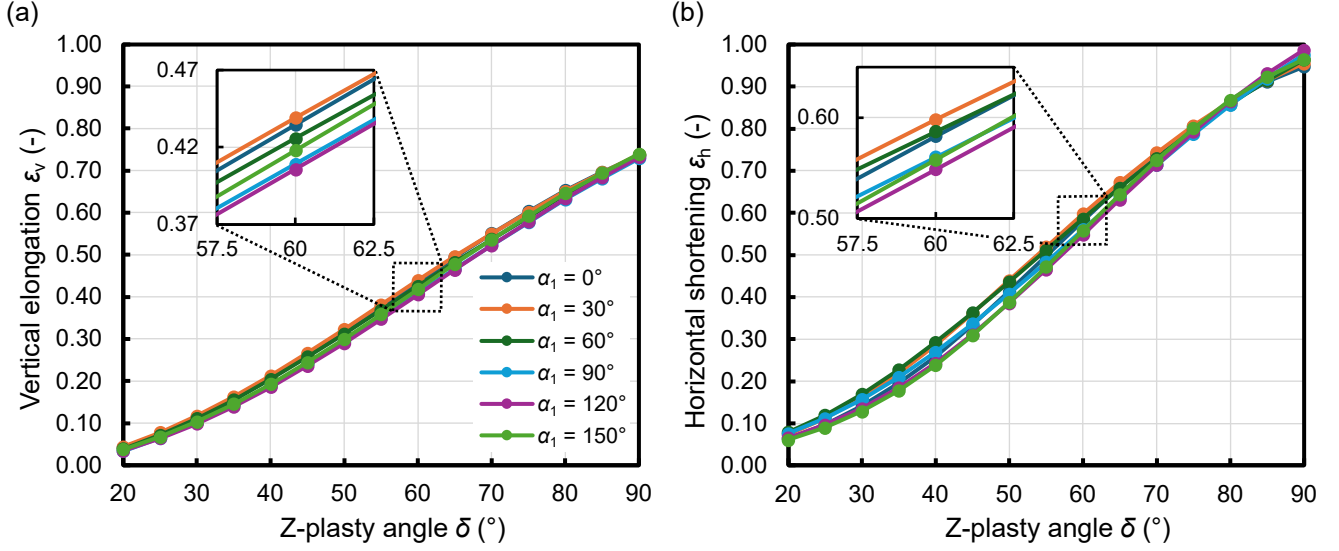


Figure 9. Vertical elongation and horizontal shortening strains in relation to the Z-plasty angle δ for the mean fiber direction angles $\alpha_1 = 0^\circ, 30^\circ, 60^\circ, 90^\circ, 120^\circ, 150^\circ$. (a) Vertical elongation strain ε_v ; (b) horizontal shortening strain ε_h . Magnifications are shown for the special case of $\delta = 60^\circ$ Z-plasty.

$\|\mathbf{X}_D - \mathbf{X}_C\|$ would reduce the objectivity of ε_h . Instead, $\|\Delta\mathbf{X}_v\|$ represents the initial scar length, which is constant for all the surgeries analyzed, hence enabling an appropriate comparison between the models.

The two strain measures are reported in Fig. 9 for all the fiber orientations α_1 analyzed. The vertical elongation strain ε_v in Fig. 9(a) is always greater than zero and increases almost linearly with δ , ranging from $3.3 \div 4.4\%$ at $\delta = 20^\circ$ to $79.2 \div 73.9\%$ at $\delta = 90^\circ$. This indicates that the surgical procedures consistently produce a lengthening effect. Concerning the horizontal shortening strain ε_h , shown in Fig. 9(b), the trends are analogous to the vertical elongation in Fig. 9(b), showing an approximately linear trend for all the angles α_1 . The values span from $6.1 \div 8.0\%$ at $\delta = 20^\circ$ to $94.8 \div 98.7\%$ at $\delta = 90^\circ$. Interestingly, both the strains seem to be almost unaffected by the mean fiber direction α_1 , with ε_v and ε_h showing only 2.4% and 3.8% difference between maximum and minimum values on average, respectively. However, it is worth noticing that the vertical elongation ε_v is always lower than the horizontal shortening ε_h as the Z-plasty angle δ varies. This trend becomes particularly evident at higher angles, where the initial distance between points C and D in the reference configuration significantly exceeds the scar length l (see geometrical scheme in Fig. 8(a)). Following the transposition, points C and D align along the central limb, corresponding to the joined sides of the two triangular flaps initially sized l , meaning that $\|\Delta\mathbf{x}_h\| \approx l$. Consequently, the deformation ε_h , being proportional to $(\Delta\mathbf{X}_h - \Delta\mathbf{x}_h) \cdot \mathbf{E}_1 \approx \|\Delta\mathbf{X}_h\| - \|\Delta\mathbf{x}_h\| \approx \|\Delta\mathbf{X}_h\| - l$, attains high values when the initial distance $\|\Delta\mathbf{X}_h\|$ between points C and D is much larger than l . Clinically, while higher strains ε_v are desirable, the horizontal strains ε_h should be reduced as much as possible in order to reduce stresses. Therefore, selecting higher angles δ to increase the elongation is a choice that must be taken carefully.

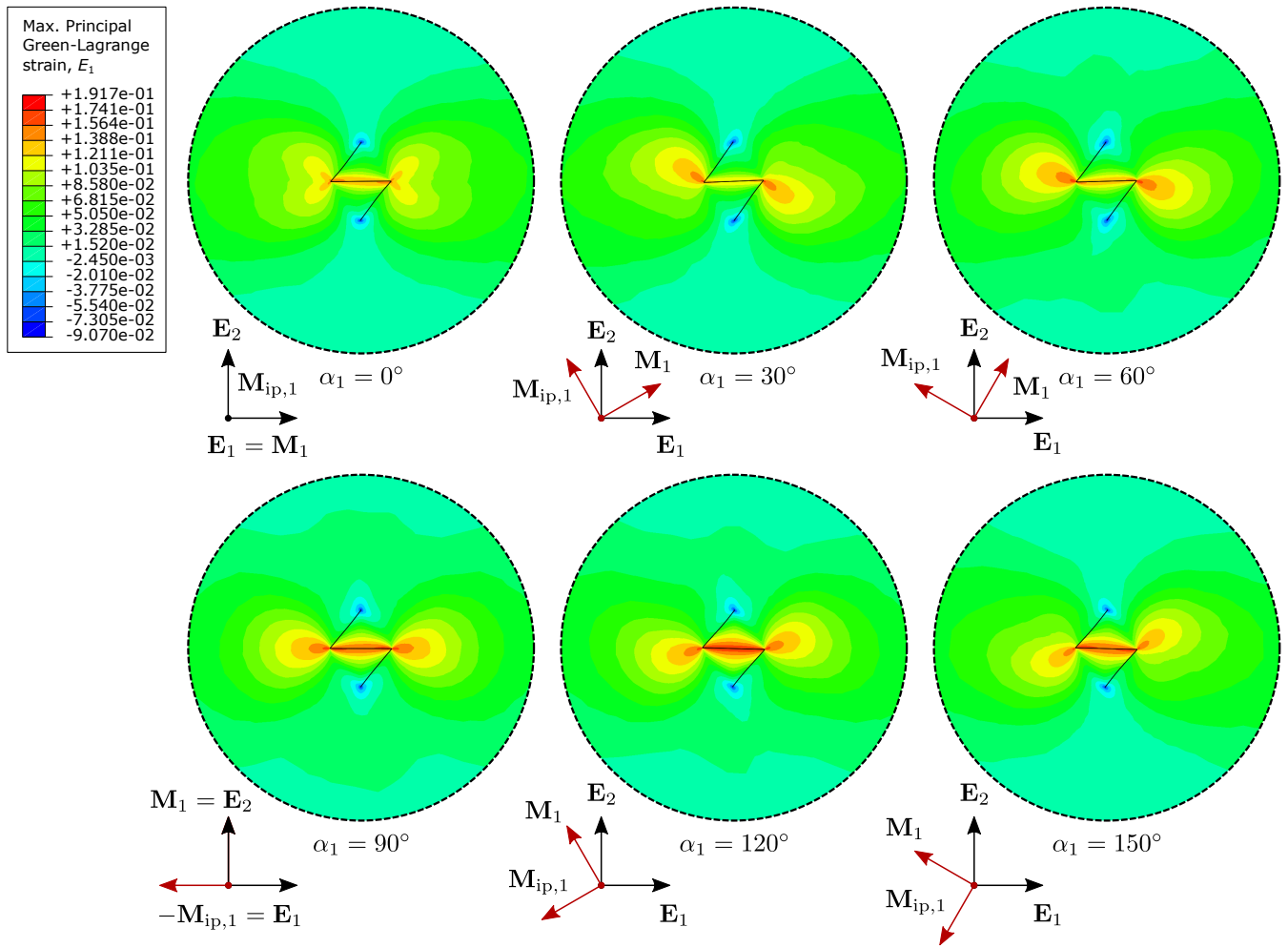


Figure 10. Maps of the maximum principal in-plane component E_1 ($> E_2, E_3$) of the Green-Lagrange strain tensor in the final configuration, for the $\delta = 60^\circ$ Z-plasty with the different mean in-plane fiber orientations α_1 . Maps are cropped to $R = 150$ mm to improve readability.

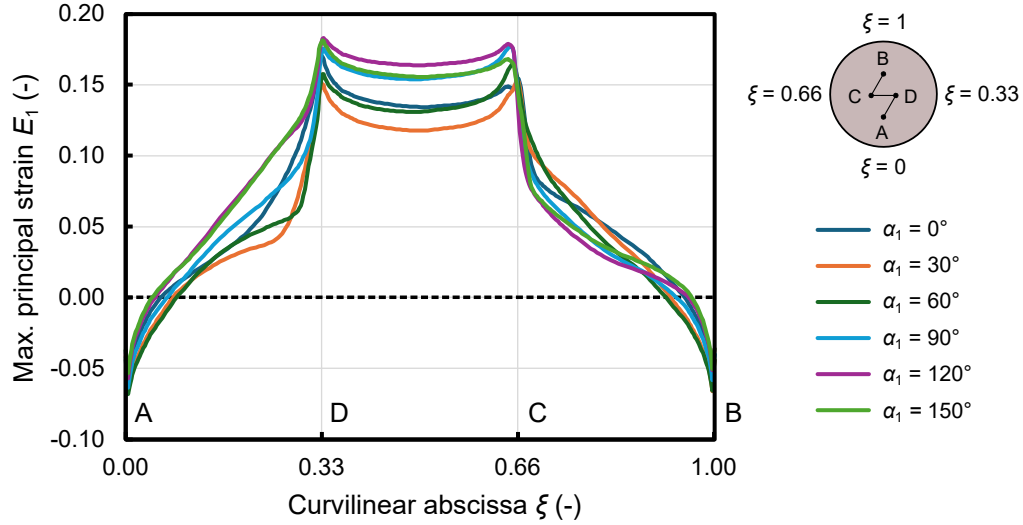


Figure 11. Maximum principal in-plane strain component E_1 along the suture for the Z-plasty case $\delta = 60^\circ$. The curvilinear abscissa $\xi = L/L_s$, $\xi \in [0, 1]$ represents the distance L from the point A at the lower end of the suture normalized with respect to the global length of the suture L_s in the final configuration.

The influence of anisotropy can be clearly appreciated from the distribution of the strains in the final configuration. Figure 10 illustrates the map of the maximum principal in-plane component E_1 of the Green-Lagrange strain tensor $\mathbf{E} = 1/2(\mathbf{C} - \mathbf{I})$ for the different mean fiber directions α_1 considered. Due to the anisotropy of the material, the lobes lateral to the points C and D tend to align with the direction $\mathbf{M}_{ip,i}$ perpendicular to the fibers (red to yellow shades in Fig. 10). This happens because the material tends to redistribute the increased horizontal strains, concentrated across the middle limb, toward the neighboring regions in the direction with lower stiffness.

A representative profile of the maximum principal in-plane strain E_1 along the suture is depicted in Fig. 11 for $\delta = 60^\circ$. The curves exhibit negative strains in the proximity of the suture ends, corresponding to the points A and B, while two peaks emerges close to the geometrical singularities located at points C and D. Between the latter, the strain remains high, indicating that the central limb is significantly more stressed than the others.

Figure 12(a) shows the peak principal strains $E_{1,p}$ from all the maximum strain E_1 profiles in relation to the Z-plasty angle δ . The plots, starting from strains of $8.8 \div 12.0\%$ at $\delta = 20^\circ$, tend to increase with decreasing slope, ending at values of $17.0 \div 20.2\%$ at $\delta = 90^\circ$. Even though the curves seem to overlap randomly, they reveal a correlation between the mean fiber orientation α_1 and the flap angle δ . By observing the plots in Fig. 12(b) showing the angles α_1 that minimize $E_{1,p}$, we observe that the minimum peak strain occurs when the fibers in the reference configuration are approximately parallel to the lateral incisions AD and BC, i.e. when $\alpha_1 = 90^\circ - \delta$. In fact, the sides of the triangular flaps initially laying on the lateral incisions occupy the central limb once the suture is closed. Therefore, when the conditions

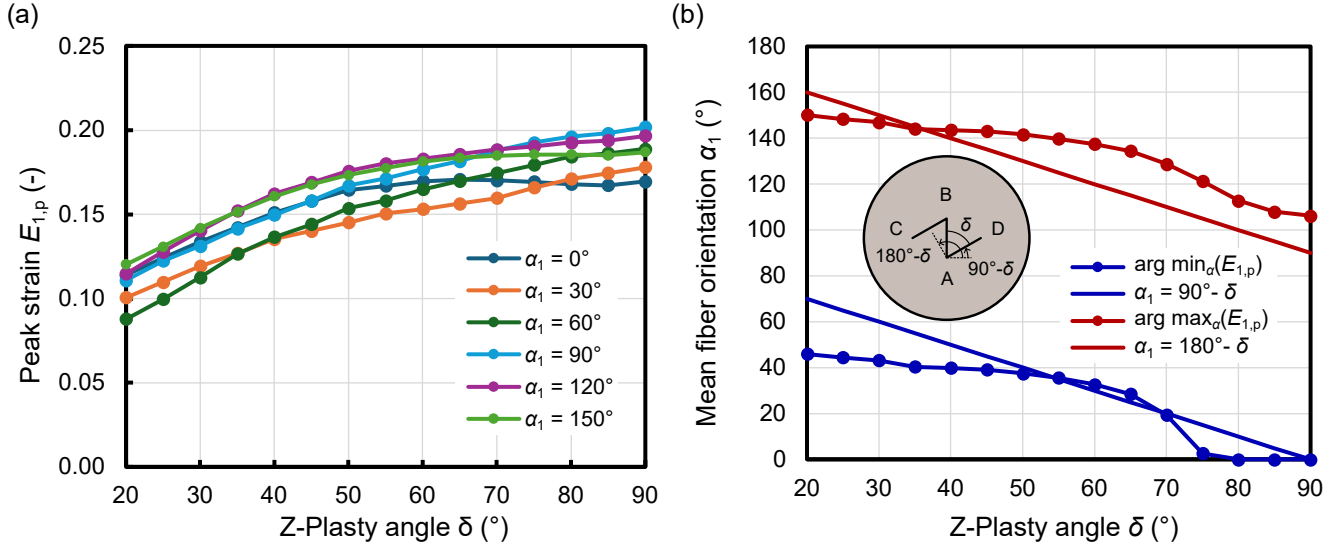


Figure 12. Peak strain analysis. (a) Peak strain $E_{1,p}$ along the suture for the different Z-plasty angle δ and mean fiber direction α_1 . (b) Mechanical and geometrical relationships between the angles δ and α_1 . The angles $\alpha_{1,\min}$ and $\alpha_{1,\max}$, minimizing and maximizing $E_{1,p}$ respectively, are obtained from the third degree polynomial fitting of the plots in (a) along α_1 for every angle δ .

$\alpha_1 = 90^\circ - \delta$ is achieved, the fibers can exert the maximum stiffness, thus reducing the strain. Conversely, when the fibers lay at right angle to the lateral limbs in the reference configuration the triangular flap has lower stiffness along the central limb, leading to increased strains.

5. Discussion

Discrete fiber dispersion models are approximation of the continuous fiber dispersion approach, offering comparable versatility for modeling the complex mechanical behavior of general fiber distributions at lower computational cost. The discrete approach enables a straightforward exclusion of fibers under compression by means of the single-fiber strain-energy in Eq. (8). As a result, the mechanical response is governed solely by the integration points N_j under tension and the ground matrix subjected to arbitrary finite deformations.

In this study, considering the relevant works of Ehret et al. [20], Skacel and Bursa [21] which compared different integration schemes, we studied a DFD model with Lebedev quadrature. The model has been implemented in the commercial FE software Abaqus for general three-dimensional formulation as well as for plane stress problems. The main advantage of the Lebedev quadrature is that the integrations points N_j are built on the unit sphere leveraging the octahedral symmetries, so that a uniform distribution of spherical point grid is obtained. In addition, the non-negativity of weights w_j preserves the poly-convexity of the strain-energy function in Eq. (7).

To reduce the computational effort, we limited the integration to one hemisphere by exploiting the

fiber symmetry $\rho_i(\mathbf{N}) = \rho_i(-\mathbf{N})$. Additionally, we excluded directions \mathbf{N}_j with negligible influence, specifically those with values $\varrho_{i,j}$ smaller than 10^{-6} . This operation sensibly reduces the number of integration points, especially when concentrations parameters a_i and b_i increase. However, the sharpness of the distribution ρ_i is limited by the quadrature order. In fact, quadrature schemes are designed to exactly integrate all the spherical harmonics up to a determined and finite degree. Therefore, when the integrand function cannot be approximated by a combination of harmonics with degree lower than the quadrature order the accuracy of the result is not guaranteed. In the limit case where the PDF becomes singular, discrete integrations can no longer be used. Recalling the integrand in Eq. (7), and the in-plane and out-of-plane distributions in Eqs. (5) and (6), respectively, this happens when either a_i and b_i approach zero. In particular, $\rho_i(\mathbf{N})$ degenerates to a Dirac delta function in the direction of \mathbf{M}_i for $a_i, b_i \rightarrow \infty$, $\rho_i(\mathbf{N}) = \delta(\|\mathbf{N} - \mathbf{M}_i\|)$, or to a singular planar distribution in the plane $\{\mathbf{M}_i, \mathbf{M}_{\text{ip},i}\}$ for $b_i \rightarrow \infty$, $\rho_i(\mathbf{N}) = \rho_{\text{ip},i}(\mathbf{N}) \delta(\mathbf{N} \cdot \mathbf{M}_{\text{op},i})$.

One way to address this issue is by setting a limit for the parameters a_i and b_i , beyond which the fiber distribution can be considered perfectly aligned, and the DFD model can be replaced by the simpler Holzapfel et al. [37] model. Likewise, when only b_i exceeds the limit, the distribution can be assumed as perfectly planar, $\rho_i(\mathbf{N}) = \rho_{\text{ip},i}$, and Eq. (7) can be reduced to an integral over the circle in the plane $\{\mathbf{M}_i, \mathbf{M}_{\text{ip},i}\}$ and solved using a simple univariate Gauss quadrature. Skacel and Bursa [21] proposed to limit the concentration to $b_i \leq 20$ using $n = 160$ integration points, but they considered a transversely isotropic fiber distribution only. For a comprehensive analysis, more values of a_i and b_i should be explored, taking also into account more complex loading configurations. However, this type of investigation goes beyond the scope of our work, which was focused on assessing the computational performance of the Lebedev quadrature in applications related to large deformation problems.

Another cause of discontinuity of the integrand function is the compression switch incorporated in the single-fiber strain-energy shown in Eq. (8). By juxtaposing the convergence rates obtained in Fig. 4(b) and Fig. 5(b), it seems that the simple shear test, despite most of the fibers were loaded in compression, converges with a rate similar to the uniaxial test, in which most of the fibers are loaded in tension. Therefore, we can conclude that the discontinuity related to the compression switch does not significantly impact the integration accuracy.

The analysis of the annular disk torsion in Section 3.3, as predicted by the observations of Ehret et al. [20], revealed that the discrete integration can lead to strongly anisotropic results for isotropic fiber distributions if an insufficient number of integration points is used. Such anisotropy arises from the intrinsic limitation of quadrature rules in exactly integrating a function under general rigid rotations of the integration points. The Lebedev quadrature rule, unlike other schemes, is invariant under the octahedral rotation group, but not for general rotations. Nonetheless, the isotropic disk approaches the expected axially symmetric solution for increasing number of integration points. The rapid convergence shown in Fig. 7(c) is likely due to the uniform distribution of the points as depicted in Fig. 3. This suggests that similar quadratures based on higher polyhedral symmetries, such as that proposed by Ahrens and Beylkin

[51], could converge even faster than Lebedev's.

Based on the convergence analyses presented in Section 3 for concentrations $0 \leq a_1 \leq 2.06$ and $b_1 = 12.36$, it turned out that the Lebedev quadrature provides accurate results using the set with $n = 217$ points on the hemisphere. This number can be further reduced by neglecting the points with $q_{i,j} = w_j \rho_i(\mathbf{N}_j) < 10^{-6}$, without significantly altering the accuracy.

Once defined the required number of integration points, we included the DFD model with Lebedev quadrature in a simulation of a corrective skin surgical technique, and analyzed its mechanical properties. In particular, we simulated a Z-plasty for different geometrical configurations of the initial incision, varying the angle δ between the vertical and lateral cuts from 20° to 90° . Moreover, we explored the influence of the material anisotropy considering different orientation of the mean fiber direction \mathbf{M}_i in the plane $\{\mathbf{E}_1, \mathbf{E}_2\}$ by changing the angle α_1 .

The analyses revealed that the vertical elongation ε_v and the horizontal shortening ε_h , see Fig. 9, are almost unaffected by the mean fiber orientation. Moreover, the relation with the Z-plasty angle δ is almost linear for both the measures. The strains spans in the interval $20^\circ \leq \delta \leq 90^\circ$ from $3.3 \div 4.4\%$ to $79.2 \div 73.9\%$ for ε_v , and from $6.1 \div 8.0\%$ to $94.8 \div 98.7\%$ for ε_h . Interestingly, these results are in agreement with our preliminary isotropic analysis in Spagnoli et al. [52], in which the strain ε_v ranged from $\sim 5\%$ to $\sim 73\%$ for the same investigated domain of the angle δ . This suggest that the Z-plasty has some intrinsic geometrical properties independent of the material anisotropy, at least in the range of parameters considered. This result appears particularly useful for the surgical practice, since it simplifies the selection of the angle δ depending on the desired ε_v to achieve, and regardless the material properties.

The effects of anisotropy, however, can be observed in the map of the maximum principal Green-Lagrange strain E_1 in Fig. 10 and in its profile along the suture in Fig. 11 for the representative Z-plasty with $\delta = 60^\circ$. The strain E_1 is negative near the suture ends and reaches its peak at points C and D. The central limb experiences higher strain, indicating a higher stress level compared to that in the lateral limbs. The analysis of the peak principal strain $E_{1,p}$ in Fig. 12(a) revealed a relationship between the mean fiber orientation α_1 and the Z-plasty angle δ . In particular, the minimum strain $E_{1,p}$ occurs when the fibers run parallel to the lateral incisions AD and BC in the initial configuration, i.e. $\alpha_1 = 90^\circ - \delta$, while the maximum occurs when the fibers are perpendicular to the lateral incisions, i.e. $\alpha_1 = 180^\circ - \delta$.

The results herein presented, however, are limited to only one set of mechanical and microstructural parameters averaged from test on human abdominal skin [5]. To demonstrate whether the Z-plasty has intrinsic geometrical properties, different set of parameters should be considered, analyzing the influence of both the mechanical and microstructural parameters. This type of analysis, such as that performed by Stowers et al. [34] on various skin surgical procedures, could also reveal further relationships between the geometry and the fiber orientation, enabling a deep understanding of this surgical procedure. This could also pave the way for the development of innovative patient-oriented surgical strategies.

6. Conclusions

In this work we analyzed the computational efficiency of a Discrete Fiber Dispersion (DFD) model integrated with the Lebedev quadrature rule. The model has been implemented in the commercial FE software Abaqus for perfectly incompressible materials in plane stress formulation. The model effectively excludes fibers under compression and provides accurate results using $n = 217$ integration points.

The DFD model was then used for a parametric analysis of the mechanical behavior of the Z-plasty surgery. The results showed that the mean fiber direction has little effects on the Z-plasty lengthening outcome, but significantly influences the maximum strain measured in proximity of the suture. Specifically, the maximum strain is minimized when the mean fiber direction is parallel to the lateral cuts in the reference configuration. These results, although limited to one set of mechanical and microstructural parameters of human skin, provided insight about the mechanical performances of the Z-plasty, strengthening the understanding of this widespread corrective surgery.

References

- [1] J. M. Benítez, F. J. Montáns, The mechanical behavior of skin: Structures and models for the finite element analysis, *Computers & Structures* 190 (2017) 75–107. doi:[10.1016/j.compstruc.2017.05.003](https://doi.org/10.1016/j.compstruc.2017.05.003).
- [2] V. Ayyalasomayajula, B. Pierrat, P. Badel, A computational model for understanding the micro-mechanics of collagen fiber network in the tunica adventitia, *Biomechanics and Modeling in Mechanobiology* 18 (2019) 1507–1528. doi:[10.1007/s10237-019-01161-1](https://doi.org/10.1007/s10237-019-01161-1).
- [3] M. J. Sadeghinia, B. Skallerud, G. A. Holzapfel, V. Prot, Biomechanics of mitral valve leaflets: Second harmonic generation microscopy, biaxial mechanical tests and tissue modeling, *Acta Biomaterialia* 141 (2022) 244–254. doi:[10.1016/j.actbio.2022.01.003](https://doi.org/10.1016/j.actbio.2022.01.003).
- [4] C. S. Holzer, A. Pukaluk, C. Viertler, P. Regitnig, A. W. Caulk, M. Eschbach, E. M. Contini, G. A. Holzapfel, Biomechanical characterization of the passive porcine stomach, *Acta Biomaterialia* 173 (2024) 167–183. doi:[10.1016/j.actbio.2023.11.008](https://doi.org/10.1016/j.actbio.2023.11.008).
- [5] R. Alberini, A. Spagnoli, M. J. Sadeghinia, B. Skallerud, M. Terzano, G. A. Holzapfel, Second harmonic generation microscopy, biaxial mechanical tests and fiber dispersion models in human skin biomechanics, *Acta Biomaterialia* 185 (2024) 266–280. doi:[10.1016/j.actbio.2024.07.026](https://doi.org/10.1016/j.actbio.2024.07.026).
- [6] G. A. Holzapfel, R. W. Ogden, S. Sherifova, On fibre dispersion modelling of soft biological tissues: A review, *Proceedings of the Royal Society A: Mathematical, Physical and Engineering Sciences* 475 (2019) 20180736. doi:[10.1098/rspa.2018.0736](https://doi.org/10.1098/rspa.2018.0736).

- [7] J. Merodio, R. Ogden, Mechanical response of fiber-reinforced incompressible non-linearly elastic solids, *International Journal of Non-Linear Mechanics* 40 (2005) 213–227. doi:[10.1016/j.ijnonlinmec.2004.05.003](https://doi.org/10.1016/j.ijnonlinmec.2004.05.003).
- [8] T. C. Gasser, R. W. Ogden, G. A. Holzapfel, Hyperelastic modelling of arterial layers with distributed collagen fibre orientations, *Journal of The Royal Society Interface* 3 (2006) 15–35. doi:[10.1098/rsif.2005.0073](https://doi.org/10.1098/rsif.2005.0073).
- [9] G. A. Holzapfel, J. A. Niestrawska, R. W. Ogden, A. J. Reinisch, A. J. Schriefl, Modelling non-symmetric collagen fibre dispersion in arterial walls, *Journal of The Royal Society Interface* 12 (2015) 20150188. doi:[10.1098/rsif.2015.0188](https://doi.org/10.1098/rsif.2015.0188).
- [10] M. Latorre, F. J. Montáns, On the tension-compression switch of the Gasser–Ogden–Holzapfel model: Analysis and a new pre-integrated proposal, *Journal of the Mechanical Behavior of Biomedical Materials* 57 (2016) 175–189. doi:[10.1016/J.JMBBM.2015.11.018](https://doi.org/10.1016/J.JMBBM.2015.11.018).
- [11] A. V. Melnik, H. Borja Da Rocha, A. Goriely, On the modeling of fiber dispersion in fiber-reinforced elastic materials, *International Journal of Non-Linear Mechanics* 75 (2015) 92–106. doi:[10.1016/j.ijnonlinmec.2014.10.006](https://doi.org/10.1016/j.ijnonlinmec.2014.10.006).
- [12] K. Li, R. W. Ogden, G. A. Holzapfel, Modeling fibrous biological tissues with a general invariant that excludes compressed fibers, *Journal of the Mechanics and Physics of Solids* 110 (2018) 38–53. doi:[10.1016/j.jmps.2017.09.005](https://doi.org/10.1016/j.jmps.2017.09.005).
- [13] K. Li, R. W. Ogden, G. A. Holzapfel, A discrete fibre dispersion method for excluding fibres under compression in the modelling of fibrous tissues, *Journal of The Royal Society Interface* 15 (2018) 20170766. doi:[10.1098/rsif.2017.0766](https://doi.org/10.1098/rsif.2017.0766).
- [14] M. Rolf-Pissarczyk, M. P. Wollner, D. R. Q. Pacheco, G. A. Holzapfel, Efficient computational modelling of smooth muscle orientation and function in the aorta, *Proceedings of the Royal Society A: Mathematical, Physical and Engineering Sciences* 477 (2021). doi:[10.1098/rspa.2021.0592](https://doi.org/10.1098/rspa.2021.0592).
- [15] M. Itskov, On the accuracy of numerical integration over the unit sphere applied to full network models, *Computational Mechanics* 57 (2016) 859–865. doi:[10.1007/s00466-016-1265-3](https://doi.org/10.1007/s00466-016-1265-3).
- [16] P. Bažant, B. H. Oh, Efficient Numerical Integration on the Surface of a Sphere, *ZAMM - Journal of Applied Mathematics and Mechanics / Zeitschrift für Angewandte Mathematik und Mechanik* 66 (1986) 37–49. doi:[10.1002/zamm.19860660108](https://doi.org/10.1002/zamm.19860660108).
- [17] J. Fliege, U. Maier, The distribution of points on the sphere and corresponding cubature formulae, *IMA Journal of Numerical Analysis* 19 (1999) 317–334. doi:[10.1093/imanum/19.2.317](https://doi.org/10.1093/imanum/19.2.317).

- [18] S. Heo, Y. Xu, Constructing fully symmetric cubature formulae for the sphere, *Mathematics of Computation* 70 (2000) 269–279. doi:[10.1090/S0025-5718-00-01198-4](https://doi.org/10.1090/S0025-5718-00-01198-4).
- [19] P. G. Ciarlet, *Mathematical Elasticity. Volume 1: Three-Dimensional Elasticity*, Elsevier Science, Amsterdam, 1988.
- [20] A. E. Ehret, M. Itskov, H. Schmid, Numerical integration on the sphere and its effect on the material symmetry of constitutive equations-A comparative study, *International Journal for Numerical Methods in Engineering* 81 (2010) 189–206. doi:[10.1002/nme.2688](https://doi.org/10.1002/nme.2688).
- [21] P. Skacel, J. Bursa, Numerical implementation of constitutive model for arterial layers with distributed collagen fibre orientations, *Computer Methods in Biomechanics and Biomedical Engineering* 18 (2015) 816–828. doi:[10.1080/10255842.2013.847928](https://doi.org/10.1080/10255842.2013.847928).
- [22] V. Alastrué, M. Martínez, M. Doblaré, A. Menzel, Anisotropic micro-sphere-based finite elasticity applied to blood vessel modelling, *Journal of the Mechanics and Physics of Solids* 57 (2009) 178–203. doi:[10.1016/j.jmps.2008.09.005](https://doi.org/10.1016/j.jmps.2008.09.005).
- [23] B. R. Britt, A. E. Ehret, Univariate Gauss quadrature for structural modelling of tissues and materials with distributed fibres, *Computer Methods in Applied Mechanics and Engineering* 415 (2023) 116281. doi:[10.1016/j.cma.2023.116281](https://doi.org/10.1016/j.cma.2023.116281).
- [24] V. I. Lebedev, Spherical quadrature formulas exact to orders 25-29, *Siberian Mathematical Journal* 18 (1977) 99–107. doi:[10.1007/BF00966954](https://doi.org/10.1007/BF00966954).
- [25] V. I. Lebedev, D. N. Laikov, A quadrature formula for the sphere of the 131st algebraic order of accuracy, in: *Doklady Mathematics*, volume 59, Pleiades Publishing, Ltd., 1999, pp. 477–481.
- [26] Dassault Systèmes SIMULIA, *Abaqus 2018, Documentation*, 2018.
- [27] C. R. Hove, E. F. Williams, III, B. J. Rodgers, Z-Plasty: A Concise Review, *Facial Plastic Surgery* 17 (2001) 289–294. doi:[10.1055/s-2001-18828](https://doi.org/10.1055/s-2001-18828).
- [28] S. R. Baker, *Local Flaps in Facial Reconstruction*, Elsevier Inc., 2007.
- [29] R. J. Rohrich, I. Ross Zbar, A SIMPLIFIED ALGORITHM FOR THE USE OF Z-PLASTY, *Plastic and Reconstructive Surgery* 103 (1999) 1513–1517.
- [30] T. Humphreys, *Cutaneous Flaps*, in: *Skin Cancer Management*, Springer New York, New York, NY, 2009, pp. 153–178. doi:[10.1007/978-0-387-88495-0_12](https://doi.org/10.1007/978-0-387-88495-0_12).
- [31] G. Hundeshagen, R. Zapata-Sirvent, J. Goverman, L. K. Branski, Tissue Rearrangements, *Clinics in Plastic Surgery* 44 (2017) 805–812. doi:[10.1016/j.cps.2017.05.011](https://doi.org/10.1016/j.cps.2017.05.011).

- [32] J. E. Leedy, J. E. Janis, R. J. Rohrich, Reconstruction of Acquired Scalp Defects: An Algorithmic Approach, *Plastic and Reconstructive Surgery* 116 (2005) 54e–72e. doi:[10.1097/01.prs.0000179188.25019.6c](https://doi.org/10.1097/01.prs.0000179188.25019.6c).
- [33] A. Buganza Tepole, A. K. Gosain, E. Kuhl, Computational modeling of skin: Using stress profiles as predictor for tissue necrosis in reconstructive surgery, *Computers & Structures* 143 (2014) 32–39. doi:[10.1016/j.compstruc.2014.07.004](https://doi.org/10.1016/j.compstruc.2014.07.004).
- [34] C. Stowers, T. Lee, I. Billionis, A. K. Gosain, A. B. Tepole, Improving reconstructive surgery design using Gaussian process surrogates to capture material behavior uncertainty, *Journal of the Mechanical Behavior of Biomedical Materials* 118 (2021) 104340. doi:[10.1016/j.jmbbm.2021.104340](https://doi.org/10.1016/j.jmbbm.2021.104340). arXiv:2010.02800.
- [35] J. A. Niestrawska, C. Viertler, P. Regitnig, T. U. Cohnert, G. Sommer, G. A. Holzapfel, Microstructure and mechanics of healthy and aneurysmatic abdominal aortas: Experimental analysis and modelling, *Journal of The Royal Society Interface* 13 (2016) 20160620. doi:[10.1098/rsif.2016.0620](https://doi.org/10.1098/rsif.2016.0620).
- [36] R. Alberini, A. Spagnoli, M. J. Sadeghinia, B. Skallerud, M. Terzano, G. A. Holzapfel, Fourier transform-based method for quantifying the three-dimensional orientation distribution of fibrous units, *Scientific Reports* 14 (2024) 1999. doi:[10.1038/s41598-024-51550-5](https://doi.org/10.1038/s41598-024-51550-5).
- [37] G. A. Holzapfel, T. C. Gasser, R. W. Ogden, A New Constitutive Framework for Arterial Wall Mechanics and a Comparative Study of Material Models, *Journal of elasticity and the physical science of solids* 2000 61:1 61 (2000) 1–48. doi:[10.1023/a:1010835316564](https://doi.org/10.1023/a:1010835316564).
- [38] A. Pissarenko, M. A. Meyers, The materials science of skin: Analysis, characterization, and modeling, *Progress in Materials Science* 110 (2020) 100634. doi:[10.1016/j.pmatsci.2019.100634](https://doi.org/10.1016/j.pmatsci.2019.100634).
- [39] J. Kiendl, M.-C. Hsu, M. C. Wu, A. Reali, Isogeometric Kirchhoff–Love shell formulations for general hyperelastic materials, *Computer Methods in Applied Mechanics and Engineering* 291 (2015) 280–303. doi:[10.1016/j.cma.2015.03.010](https://doi.org/10.1016/j.cma.2015.03.010).
- [40] G. Holzapfel, *Nonlinear Solid Mechanics: A Continuum Approach for Engineering Science*, volume 37, John Wiley & Sons, 2000. doi:[10.1023/A:1020843529530](https://doi.org/10.1023/A:1020843529530).
- [41] M. A. Crisfield, *Non-Linear Finite Element Analysis of Solids and Structures - Volume II*, John Wiley & Sons, Ltd, Chichester, UK, 1996.
- [42] V. Prot, B. Skallerud, G. A. Holzapfel, Transversely isotropic membrane shells with application to mitral valve mechanics. Constitutive modelling and finite element implementation, *International Journal for Numerical Methods in Engineering* 71 (2007) 987–1008. doi:[10.1002/nme.1983](https://doi.org/10.1002/nme.1983).

- [43] M. Palizi, S. Federico, S. Adeb, Consistent numerical implementation of hypoelastic constitutive models, *Zeitschrift für angewandte Mathematik und Physik* 71 (2020) 156. doi:[10.1007/s00033-020-01335-3](https://doi.org/10.1007/s00033-020-01335-3).
- [44] S. Zhang, J. Jin, *Computation of Special Functions*, Wiley, 1996.
- [45] C. H. L. Beentjes, Quadrature on a Spherical Surface, *International Conference on Mathematics and Computational Methods Applied to Nuclear Science and Engineering* (2015) 1–15.
- [46] K. Li, R. W. Ogden, G. A. Holzapfel, Computational method for excluding fibers under compression in modeling soft fibrous solids, *European Journal of Mechanics - A/Solids* 57 (2016) 178–193. doi:[10.1016/j.euromechsol.2015.11.003](https://doi.org/10.1016/j.euromechsol.2015.11.003).
- [47] D. W. Furnas, G. W. Fischer, The Z-plasty: Biomechanics and mathematics, *British Journal of Plastic Surgery* 24 (1971) 144–160. doi:[10.1016/S0007-1226\(71\)80034-6](https://doi.org/10.1016/S0007-1226(71)80034-6).
- [48] T. Gibson, R. Kenedi, Biomechanical Properties of Skin, *Surgical Clinics of North America* 47 (1967) 279–294. doi:[10.1016/S0039-6109\(16\)38180-4](https://doi.org/10.1016/S0039-6109(16)38180-4).
- [49] W. F. Larrabee, G. A. Holloway, D. Sutton, Wound Tension and Blood Flow in Skin Flaps, *Annals of Otology, Rhinology & Laryngology* 93 (1984) 112–115. doi:[10.1177/000348948409300202](https://doi.org/10.1177/000348948409300202).
- [50] R. Alberini, A. Spagnoli, M. Terzano, Numerical modelling of wrinkled hyperelastic membranes with topologically complex internal boundary conditions, *International Journal of Mechanical Sciences* 212 (2021) 106816. doi:[10.1016/j.ijmecsci.2021.106816](https://doi.org/10.1016/j.ijmecsci.2021.106816).
- [51] C. Ahrens, G. Beylkin, Rotationally invariant quadratures for the sphere, *Proceedings of the Royal Society A: Mathematical, Physical and Engineering Sciences* 465 (2009) 3103–3125. doi:[10.1098/rspa.2009.0104](https://doi.org/10.1098/rspa.2009.0104).
- [52] A. Spagnoli, R. Alberini, E. Raposio, M. Terzano, Simulation and optimization of reconstructive surgery procedures on human skin, *Journal of the Mechanical Behavior of Biomedical Materials* 131 (2022) 105215. doi:[10.1016/j.jmbbm.2022.105215](https://doi.org/10.1016/j.jmbbm.2022.105215).